



ARL-TR-7766 • SEP 2016



Enhancements to the Tonge-Ramesh Ceramic Failure Model for Use in Eulerian Simulations

by Andrew L Tonge

Approved for public release; distribution is unlimited.

NOTICES

Disclaimers

The findings in this report are not to be construed as an official Department of the Army position unless so designated by other authorized documents.

Citation of manufacturer's or trade names does not constitute an official endorsement or approval of the use thereof.

Destroy this report when it is no longer needed. Do not return it to the originator.



Enhancements to the Tonge-Ramesh Ceramic Failure Model for Use in Eulerian Simulations

by Andrew L Tonge

Weapons and Materials Research Directorate, ARL

REPORT DOCUMENTATION PAGE				Form Approved OMB No. 0704-0188	
<p>Public reporting burden for this collection of information is estimated to average 1 hour per response, including the time for reviewing instructions, searching existing data sources, gathering and maintaining the data needed, and completing and reviewing the collection information. Send comments regarding this burden estimate or any other aspect of this collection of information, including suggestions for reducing the burden, to Department of Defense, Washington Headquarters Services, Directorate for Information Operations and Reports (0704-0188), 1215 Jefferson Davis Highway, Suite 1204, Arlington, VA 22202-4302. Respondents should be aware that notwithstanding any other provision of law, no person shall be subject to any penalty for failing to comply with a collection of information if it does not display a currently valid OMB control number.</p> <p>PLEASE DO NOT RETURN YOUR FORM TO THE ABOVE ADDRESS.</p>					
1. REPORT DATE (DD-MM-YYYY) September 2016		2. REPORT TYPE Technical Report		3. DATES COVERED (From - To) October 2014–April 2016	
4. TITLE AND SUBTITLE Enhancements to the Tonge-Ramesh Ceramic Failure Model for Use in Eulerian Simulations				5a. CONTRACT NUMBER	
				5b. GRANT NUMBER	
				5c. PROGRAM ELEMENT NUMBER	
6. AUTHOR(S) Andrew L Tonge				5d. PROJECT NUMBER	
				5e. TASK NUMBER	
				5f. WORK UNIT NUMBER	
7. PERFORMING ORGANIZATION NAME(S) AND ADDRESS(ES) US Army Research Laboratory ATTN: RDRL-WMP-C Aberdeen Proving Ground, MD 21005-5066				8. PERFORMING ORGANIZATION REPORT NUMBER ARL-TR-7766	
9. SPONSORING/MONITORING AGENCY NAME(S) AND ADDRESS(ES)				10. SPONSOR/MONITOR'S ACRONYM(S)	
				11. SPONSOR/MONITOR'S REPORT NUMBER(S)	
12. DISTRIBUTION/AVAILABILITY STATEMENT Approved for public release; distribution is unlimited.					
13. SUPPLEMENTARY NOTES primary author's email: <andrew.l.tonge.civ@mail.mil>.					
14. ABSTRACT The Tonge-Ramesh material model has been incorporated into 3 computational frameworks (EPIC, ALE3D, and ALEGRA) used by the US Army Research Laboratory for the simulation of terminal ballistic problems. Southwest Research Institute (SwRI) report number 1817637.03 noted that in the Lagrangian code EPIC, the Tonge-Ramesh model was relatively robust but was computationally expensive compared to simpler models, like Johnson-Holmquist-Beissel, and the damaged material was too strong. This work confirms the SwRI findings when using a different numerical method and identifies further limitations of the original model when it is used in an advecting framework. A simplified version of the model that is faster, more robust, and better suited for use in codes with advection, like ALE3D, is presented in this work along with evaluations of both the original and the updated models in ALE3D.					
15. SUBJECT TERMS ceramic, damage, material model, failure, ALE3D					
16. SECURITY CLASSIFICATION OF:			17. LIMITATION OF ABSTRACT UU	18. NUMBER OF PAGES 52	19a. NAME OF RESPONSIBLE PERSON Andrew L Tonge
a. REPORT Unclassified	b. ABSTRACT Unclassified	c. THIS PAGE Unclassified			19b. TELEPHONE NUMBER (Include area code) 410-278-1069

Contents

List of Figures	v
List of Tables	vi
1. Introduction	1
2. Background	2
2.1 Original TR Model	2
2.2 TR Model with a Smooth Granular Flow Yield Surface	5
2.3 Demands Placed on a Constitutive Model by Multiple Host Codes	6
2.4 Prior Evaluations of the Model	7
3. Development of a Faster More Robust Version of the Model (TR2)	7
3.1 Elastic Response	8
3.2 Volume Preserving Inelastic Flow	10
3.3 Damage Model	10
3.4 Granular Flow	12
3.4.1 Yield Surface	13
3.4.2 Rate Dependence	16
3.5 TR2 Material Model Parameters	18
3.6 TR2 History Variables	20
3.7 Numerical Implementation	21
3.7.1 Rate Independent Projection	21
3.7.2 Rate Dependence	25
3.8 Timing Results	26
4. Model Evaluation Methods	27
4.1 Geometry from Prior Experiments	27
4.2 Simulation Mesh	27
4.3 Material Parameters	30
5. Results	32

6. Discussion	36
7. Conclusion	38
8. References	39
Distribution List	43

List of Figures

Fig. 1	Schematic of error introduced by solving the distortion flow first (A-B-C) followed by the compaction (C-D). The correct return location is E.....	5
Fig. 2	Error in the pressure calculation introduced due to a constant modulus assumption for a Mie-Grüneisen equation of state for logarithmic volume strain increments up to 0.1 and logarithmic volumetric strains of 1	9
Fig. 3	Error in the energy calculation introduced due to a constant modulus assumption for a Mie-Grüneisen equation of state for logarithmic volume strain increments up to 0.1 and logarithmic volumetric strains of 1	10
Fig. 4	Meridional profile of the granular material yield surface showing the effect of important input parameters	14
Fig. 5	Normalized octahedral profile of the granular material yield surface showing the effect of the parameter \bar{r}_e	15
Fig. 6	Comparison of single element uniaxial strain compression simulations from an initially distended state showing the effect of strain increment size	24
Fig. 7	Pressure-volume response for an initially distended material for uniaxial strain compression with a strain increment of 0.001 for the consistent algorithm and the faster nonhardening algorithm.....	25
Fig. 8	Slice view of the initial Lagrangian mesh used for the geometry 1 penetration simulations	28
Fig. 9	Representative mesh used for the Eulerian simulations of geometry 1 using 4 elements across the rod radius	29
Fig. 10	Cut view of the initial mesh used for Lagrangian simulations of geometry 3	30
Fig. 11	Comparison of simulation results for the Lagrangian simulations of geometries 1 and 2 at the end of the simulation.....	33
Fig. 12	Comparison of simulation results for the geometry 3 long rod impact geometry 60 μs after impact	34
Fig. 13	Comparison of simulation results for the Eulerian simulations of the geometry 1 long rod impact problem using the TR1a and TR2 models with material parameters fit to the JHB set B boron carbide model and an initial impact velocity of 1,480 m/s 50 μs into the simulation	36

List of Tables

Table 1	Material parameters in TR2 model.....	19
Table 2	Model specific history variables	20
Table 3	Summary of model evaluation times for 1,000 elements simulated for 1,000 timesteps.....	26
Table 4	Material parameters used in TR1 and TR1a model evaluation	31
Table 5	Summary of simulation results	32

1. Introduction

Micro-mechanics-based material models such as the Tonge-Ramesh material model¹ have the potential to connect processing details like the residual flaw distribution to simulation capabilities that can be used in the design of next-generation armor systems, with the ultimate goal of reducing the cost and lead time for developing new capabilities. These goals require an understanding of the performance of these advanced material models under conditions relevant for simulating ballistic impact events. The papers that initially presented the model demonstrated that the model can be used for impact events where there is moderate deformation of the materials using a material point method numerical scheme.^{1,2}

The model may be used for both nonpenetrating impact events, such as those investigated by Tonge and Ramesh, and impact events with very large deformations such as long-rod penetration. Since nonpenetrating impact events were addressed in the initial articles, this work focuses on the behavior of the model for events with large amounts of projectile penetration.

This report begins by summarizing the Tonge-Ramesh material model including both the original 2-surface-distortion/compaction model for granular flow and a more recent single-surface granular flow model. Following this summary, the results from the Southwest Research Institute (SwRI) effort incorporating the model into the EPIC finite element code are summarized, including their findings regarding the limitations of the model. After presenting background on the various iterations of the Tonge-Ramesh model, 2 long-rod test problem geometries are discussed. Simulations of these impact events using a Lagrangian mesh with SPH particle insertion in ALE3D are used to confirm that the model behaviors observed by SwRI are also present in an alternative numerical framework. One of the problem geometries is also simulated using an Eulerian mesh in addition to the Lagrangian simulations to assess the ability of the model to handle the errors associated with material transport. While this report only tests the updated model in ALE3D, the results should also apply if the updated model is transitioned to EPIC.

2. Background

The Tonge-Ramesh material model¹ is an isotropic micro-mechanics-based damage model designed for simulating ceramic materials subjected to impact loading. The original form of the model¹ described a material failure process that was initially dominated by micro-crack growth through a wing-cracking mechanism followed by granular flow of a comminuted material. Three different material models are discussed in this report. The models will be referenced using the following terms:

- TR1: This is the original model.
- TR1a: This model uses a smooth single surface to define the yield locus for the comminuted material.
- TR2: This model is a simplified version of the TR1a model and is described in detail in Section 3.

For completeness, the TR1 and TR1a models are described in Sections 2.1 and 2.2.

2.1 Original TR Model

The model was cast in a finite deformation framework with a multiplicative split of the deformation gradient (\mathbf{F}) into an elastic portion (\mathbf{F}_e) and an inelastic portion (\mathbf{F}_{GP}) such that $\mathbf{F} = \mathbf{F}_e \mathbf{F}_{GP}$. The model specifies the Kirchhoff stress as a combination of a deviatoric contribution ($\boldsymbol{\tau}_{dev}$) and a hydrostatic contribution ($p_s J_e \mathbf{I}$). The deviatoric contribution is linearly proportional to the deviatoric part of $\bar{\mathbf{b}}_e = J_e^{-2/3} \mathbf{F}_e \mathbf{F}_e^T$:

$$\boldsymbol{\tau}_{dev} = G \left(\bar{\mathbf{b}}_e - \frac{1}{3} \text{tr}(\bar{\mathbf{b}}_e) \mathbf{I} \right). \quad (1)$$

The shear modulus (G) decreases with damage according to an increased compliance model:

$$G(D) = \left(G_0^{-1} + \frac{2D}{15} (3Z_r + 2Z_n - 4Z_c) \right)^{-1}. \quad (2)$$

The constants Z_r , Z_n , and Z_c represent the radial, normal, and coupling compliance of a single penny-shaped crack in an isotropic elastic medium. They are functions of only the elastic moduli. The coupling term was added by Tonge and Ramesh,¹ while the other terms are based on single-crack work by Grechka and Kachanov.³ A Mie-Grüneisen equation of state is used to define the pressure p_s associated with

undamaged material without porosity

$$p_s(J^e, \theta) = p_H(J^e) \left[1 - \frac{\Gamma_0}{2} (1 - J^e) \right] + \rho_0 \Gamma_0 [e_c(J^e) + c_\eta(\theta - \theta_0)]. \quad (3)$$

Here J^e is the thermoelastic volume change ratio, Γ_0 is the Grüneisen coefficient, ρ_0 is the reference density, c_η is the specific heat, θ is the temperature, e_c is the cold energy associated with compression to J^e , and p_H is the Hugoniot pressure given by

$$p_H(J^e) = \begin{cases} \frac{\rho_0 C_0^2 (1 - J^e)}{(1 - S(1 - J^e))^2} & J^e < 1.0 \\ \rho_0 C_0^2 (1 - J^e) & \text{otherwise.} \end{cases} \quad (4)$$

Damage is incorporated into the bulk modulus according to

$$K(D) = (K_0^{-1} + D(Z_n + 4Z_c))^{-1}. \quad (5)$$

Based on the damaged bulk modulus, the pressure, including the effects of damage, the nonlinear equation of state, and temperature, is

$$p_s(J^e, \theta, D) = \frac{K(D)}{K_0} \left(p_H(J^e) \left[1 - \frac{\Gamma_0}{2} (1 - J^e) \right] + \rho_0 \Gamma_0 [e_c(J^e) + c_\eta \theta] \right). \quad (6)$$

The damage variable D is computed from the growth of a distribution of microcracks

$$D = \sum_k^{N_{\text{bins}}} \omega_k (s_k + l_k)^3. \quad (7)$$

Here ω_k is the number density of flaws within a family (or bin) of flaws. These flaws are represented by an initial flaw size, s_k , and have grown an additional length, l_k . The flaw growth rate depends on the local stress intensity factor, K_I , at the crack tip according to

$$\dot{l} = \frac{C_r}{\alpha_c} \left(\frac{K_I - K_{IC}}{K_I - 0.5K_{IC}} \right). \quad (8)$$

Once damage reaches a critical level, D_c , the granular flow phase of the material model is activated.

In the granular flow phase, there is a distortional yield surface written in terms of the Kirchoff stress ($\boldsymbol{\tau}$) defined by

$$f(\boldsymbol{\tau}) = \sqrt{\boldsymbol{\tau}_{\text{dev}} : \boldsymbol{\tau}_{\text{dev}}} - Y + A \left(\frac{\text{tr}(\boldsymbol{\tau})}{\sqrt{3}} - B \right) = 0. \quad (9)$$

The model assumes associated flow to determine the direction of inelastic deformation. The rate of inelastic deformation is determined by assuming linear viscoplastic behavior parametrized by a relaxation time τ_{GP} . The associated flow for the distortion mechanism introduces porosity. To account for pore collapse, an additional yield surface that depends on the pressure ($P = -\text{tr}(\boldsymbol{\sigma})/3$), distension (J_{GP}), and total volume change ratio (J)

$$f_{\phi}(P, J^{GP}, J) = \begin{cases} \frac{P}{P_c - P_0} - \frac{P_0}{P_c - P_0} \exp\left(-\frac{P_c - P_0}{2P_0(J_0^{GP} - 1)}(J^{GP} - J_0^{GP})\right) & P < P_0 \\ (J^{GP} - 1) - (J_0^{GP} - 1)J^2 \left(\frac{P_c - P}{P_c - P_0}\right)^2 & P_0 \leq P < P_c \\ J^{GP} - 1 & P_c < P \end{cases} \quad (10)$$

Numerically these 2 mechanisms are solved sequentially. The distortion mechanism is computed first, introducing porosity, followed by a compaction step where the porosity is reduced. This sequential solution procedure, while reasonable from an operator-splitting perspective, introduces errors when large-strain increments are introduced for loading steps near the intersection of the 2 yield surfaces. The source of the error is shown in Fig. 1. Starting from point A, which resides on the distortion yield surface, an increment in deformation results in a trial stress located at point B. From point B, the return algorithm for the distortion mechanism returns the stress to point C. The pressure at point C can be arbitrarily large because it does not account for pore collapse. The pressure could be so large that the Mie-Grüneisen equation of state cannot be inverted to separate the elastic volumetric deformation from the inelastic volume deformation. From point C, the pore compaction return algorithm takes the stress from point C to point D. The correct return location should be point E. When testing the material model in the EPIC computational code,⁴ a failure to invert the Mie-Grüneisen equation of state caused a simulation to fail at an impact velocity of 4,500 m/s.

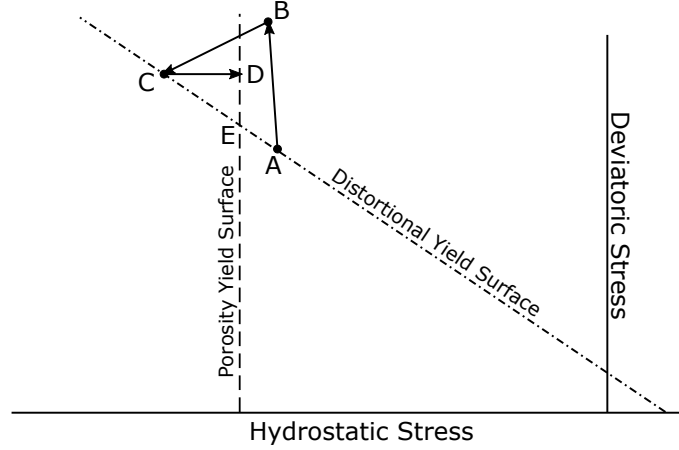


Fig. 1 Schematic of error introduced by solving the distortion flow first (A-B-C) followed by the compaction (C-D). The correct return location is E.

2.2 TR Model with a Smooth Granular Flow Yield Surface

To facilitate comparisons with other ceramic failure models, such as Johnson–Holmquist–Beissel (JHB),⁵ a unified yield surface model was incorporated to represent both the compaction and dilatation of the comminuted material using a single surface in terms of the Lode invariants. This variant of the model is referred to as TR1a.

For a Cauchy stress tensor, $\boldsymbol{\sigma}$, with a deviatoric part, $\boldsymbol{s} = \boldsymbol{\sigma} + p\boldsymbol{I}$, the Lode invariants are

$$r = \sqrt{\boldsymbol{s} : \boldsymbol{s}}, \quad (11)$$

$$z = \frac{1}{\sqrt{3}} \text{tr}(\boldsymbol{\sigma}), \quad (12)$$

$$\text{and, } \sin 3\theta = \frac{J_3}{2} \left(\frac{3}{J_2} \right)^{2/3}. \quad (13)$$

The yield function⁶ is written as

$$f(r, z, \theta, \gamma_p, \epsilon_p^v) = \Gamma(\theta)^2 \frac{1}{2} r^2 - F_f(z, \gamma_p) |F_f(z, \gamma_p)| F_c(z, \epsilon_p^v) \quad (14)$$

$$F_f(z, \gamma_p) = \left(\frac{\mu(\gamma_p)}{\mu_0} \right) \left(a_1 - a_3 \exp \left(a_2 \sqrt{3} z \right) - \mu_0 \sqrt{3} z \right) \quad (15)$$

$$F_c(z, \epsilon_p^v) = \begin{cases} 1 - \frac{(\kappa(\epsilon_p^v) - \sqrt{3} z)^2}{(\kappa(\epsilon_p^v) - X(\epsilon_p^v))^2} & \text{if } \sqrt{3} z < \kappa \\ 1 & \text{otherwise} \end{cases} \quad (16)$$

$$\mu(\gamma_p) = \mu_1 + (\mu_0 - \mu_1) \exp(-\mu_2 \gamma_p) \quad (17)$$

$$X(\epsilon_p^v) = p_1 \left(p_0 + \frac{1}{2} (\ln(p_3 + p_2 \epsilon_p^v) - |\ln(p_3 + p_2 \epsilon_p^v)|) \right) \quad (18)$$

$$\kappa(\epsilon_p^v) = p_4 X(\epsilon_p^v). \quad (19)$$

The plastic flow direction is

$$\mathbf{M} = \alpha(\mathbf{N}_{\text{dev}} + \beta \mathbf{N}_{\text{iso}}). \quad (20)$$

Here \mathbf{N}_{dev} and \mathbf{N}_{iso} are the deviatoric and isotropic parts of yield surface normal, β is an input parameter ($\beta \leq 1$), and α is a normalization parameter to ensure that $\mathbf{M} : \mathbf{M} = 1$. This granular-flow model uses the multistage return algorithm.⁷ For all of the cases investigated in this work, the Lode angle dependence is turned off and $\Gamma(\theta) = 1$. In this form of the model, the rate independent solution to the plasticity problem is tracked in addition to the rate dependent solution to provide a more accurate integration of the viscous relaxation model.⁸

2.3 Demands Placed on a Constitutive Model by Multiple Host Codes

Modeling and simulation is about providing some insight into an event based on a reasonable set of assumptions. Different tools for solving the momentum and energy balance equations, will make different assumptions and stress the material models in different ways. This work focuses on the Tonge-Ramesh model in ALE3D, which provides options to use a fully Lagrangian description of the material or introduce varying degrees of advection up to fully Eulerian calculations. For a material model, a finite deformation Lagrangian formulation is the least stressing condition, because the material history is accurately tracked.⁹ In advecting calculations, the relative motion between the material and the mesh can corrupt the history variables that are carried with the material. Some mechanism must be introduced to

deal with the massive material distortion that will eventually distort a Lagrangian mesh so severely that the accuracy is lost, elements can invert, and a simulation will crash. This work discusses the performance of the Tonge-Ramesh model in a long-rod impact problem for both Eulerian calculations and Lagrangian calculations with conversion of distorted elements to Smoothed Particle Hydrodynamics (SPH) particles.

2.4 Prior Evaluations of the Model

SwRI implemented the Tonge-Ramesh (TR1) model into the finite element code EPIC and performed a similar evaluation.⁴ EPIC is a Lagrangian finite element code with various erosion algorithms to address highly distorted elements. In simulations of various impact configurations, they concluded that the material model (TR1) was relatively robust but slow compared to other models like the JHB¹⁰ model. Of all the simulation runs that they performed, only an impact at 4,500 m/s failed to run to completion.

Additional documentation of the TR1 and TR1a models is available in the user manual for the material model.¹¹

3. Development of a Faster More Robust Version of the Model (TR2)

This section presents a second generation of the Tonge-Ramesh material model (TR2) with some simplifications and enhancements to ensure a more robust solution especially in the presence of advection errors. Even with these improvements, significant advection of material prior to failure will cause problems due to the smearing of the local flaw distributions.

An initial analysis of the TR1 and TR1a models indicated that there were 4 areas where a significant increase in execution speed or robustness may be possible without compromising the physics of the problem. They were in the following areas:

- The use of a finite deformation framework, in particular defining the deviatoric part of the elastic stresses in terms of \bar{b}^e
- The inversion of the Mie-Grüneisen equation of state
- The granular flow return algorithms

- Tracking all 9 components of symmetric rank 2 tensors in 3 dimensions when only 6 components are needed

The finite deformation framework that uses $\bar{\mathbf{b}}^e$ to define the deviatoric elastic response is important for polymer materials, where large elastic strains are possible, but may be unnecessary for ceramic materials. By assuming constant moduli during a timestep, we can eliminate the nonlinear solve used to invert the Mie-Grüneisen equation of state after computing the stress satisfying the projection back to the yield surface.

3.1 Elastic Response

The model uses an incremental formulation where the shear modulus is constant and the bulk modulus is given by the Mie-Grüneisen equation of state. It is shown here for completeness:

$$\eta = 1 - \frac{\rho_0}{\rho} \quad (21)$$

$$U_s = \frac{C_0}{1 - s_1\eta - s_2\eta^2 - s_3\eta^3} \quad (22)$$

$$\frac{dU_s}{d\eta} = \frac{C_0 (s_1 - 2s_2\eta - 3s_3\eta^2)}{(1 - s_1\eta - s_2\eta^2 - s_3\eta^3)^2} \quad (23)$$

$$P_h = \rho_0 U_s^2 \eta \quad (24)$$

$$\frac{dP_h}{d\eta} = \rho_0 U_s^2 + 2\rho_0 U_s \frac{dU_s}{d\eta} \eta \quad (25)$$

$$p = P_h (1 - 0.5\Gamma_0\eta) + \rho_0\Gamma_0 e \quad (26)$$

$$K_{\text{therm}} = \frac{dP_h}{d\eta} (1 - 0.5\Gamma_0\eta) - 0.5\Gamma_0 P_h \quad (27)$$

$$K_{\text{ise}} = K_{\text{therm}} + p\Gamma_0. \quad (28)$$

To simplify the implementation, the moduli are assumed constant over a time-step. The stress and internal energy are integrated in time; the temperature is not calculated. It can always be estimated from the total internal energy in a post processing step. For simulations using explicit time-stepping schemes, this is a reasonable approximation. Figures 2 and 3 demonstrate that while the constant modulus assumption does introduce some error in to the pressure and energy calculations, the solution converges linearly with the size of the strain increment and is the error small for strain increments of 0.01. Using equation-of-state parameters that are representative

of boron carbide and a single element driver, the pressure at a logarithmic volume strain of -0.1 was 29.46 GPa, when using 1,000 time increments. The associated stored elastic energy per unit mass was 0.5607 MJ/kg. When using a single time increment, the computed pressure is 23.22 GPa, and the associated strain energy per unit mass is 0.921 MJ/kg. This represents an error of 22% in the pressure and 81% in the strain energy per unit mass when a single step is used relative to using 1,000 steps to obtain a logarithmic volume strain of 0.1. A logarithmic volume strain increment of 0.1 with the associated increment in pressure of nearly 30 GPa is very large and one should only expect a constitutive model to produce a reasonable answer; one should not expect an accurate pressure or strain energy measure with such a large increment in volume strain.

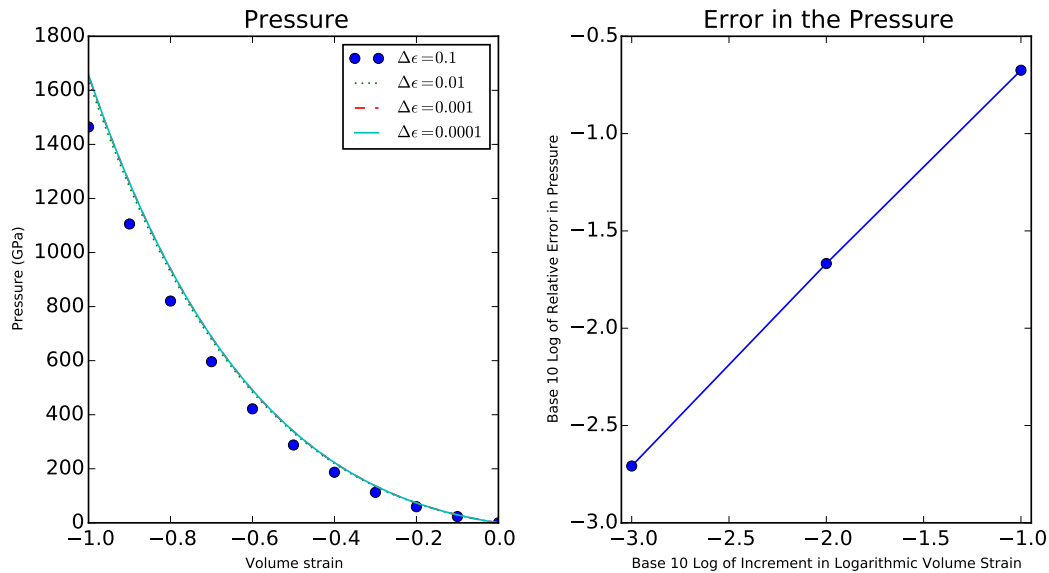


Fig. 2 Error in the pressure calculation introduced due to a constant modulus assumption for a Mie-Grüneisen equation of state for logarithmic volume strain increments up to 0.1 and logarithmic volumetric strains of 1

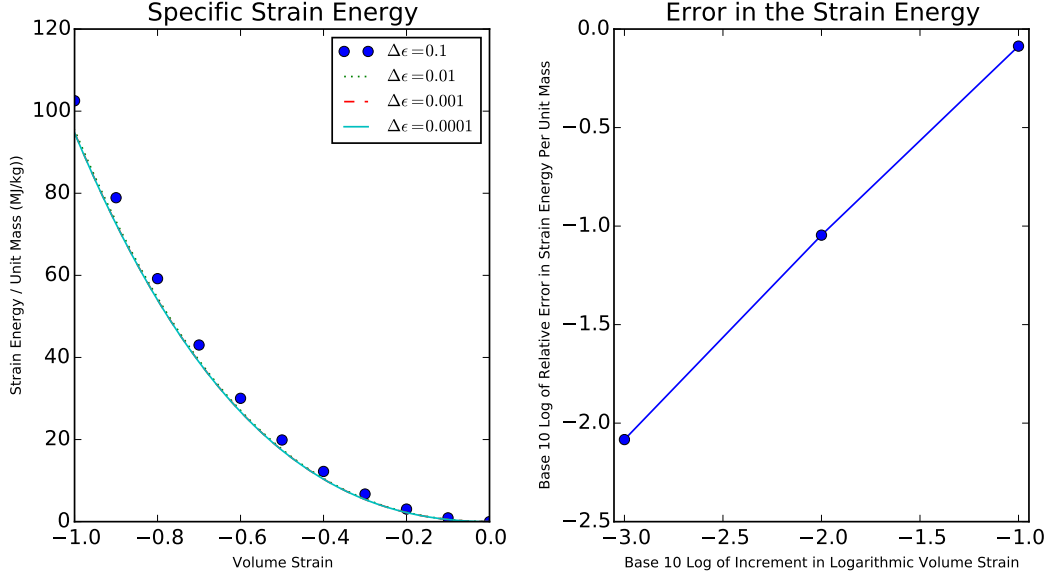


Fig. 3 Error in the energy calculation introduced due to a constant modulus assumption for a Mie-Grüneisen equation of state for logarithmic volume strain increments up to 0.1 and logarithmic volumetric strains of 1

3.2 Volume Preserving Inelastic Flow

The model allows for traditional volume preserving plasticity with a linear-hardening law and linear rate dependence. The yield surface is defined by

$$f_{J_2}(\boldsymbol{\sigma}, \epsilon_p) = \|\boldsymbol{\sigma}_{\text{dev}}\| - (H\epsilon_p + \tau_0). \quad (29)$$

Here H is the plastic hardening (or softening) modulus, ϵ_p is the accumulated plastic strain due to this deformation mechanism, and τ_0 is the initial shear strength. Optionally, a relaxation time can be provided for a Duvaut–Lions overstress viscoplasticity model.

3.3 Damage Model

The model uses an interacting micro-crack model based on a wing-cracking mechanism and handles the crack interactions using an Eshelby type self-consistent approach.¹ The effective stress in the neighborhood of a crack $\boldsymbol{\sigma}_e$ depends on both the macroscopic stress (Gauss point or material point stress, $\boldsymbol{\sigma}$) and the damage level.

Micro-crack growth is driven by the stress intensity factor (K_I) at the crack tips, which depends on both a wedging force F_w and the transverse stress normal to the wing crack faces

$$K_I = \frac{F_w}{\sqrt{\pi(l + 0.27s)}} + \sigma_{22}^e \sqrt{\pi(l + \sin(\phi)s)}. \quad (30)$$

The crack growth velocity is given by

$$\dot{l} = v_m \left(\frac{K_I - K_{IC}}{K_I + 0.5K_{IC}} \right). \quad (31)$$

Here v_m is the maximum crack growth velocity. This performs the same role as C_r/α_c in Eq. 8 but avoids the need to compute the Rayleigh wave speed at each timestep.

The crack growth velocity is a nonlinear function of the wing crack length. To minimize errors associated with finite-sized timesteps and promote smooth crack growth, we use the following semi-implicit scheme to update the crack length:

$$l_{n+1} = l_n + \Delta t \dot{l}(l_{n+1}, \sigma_n, D_n, s_{n+1}). \quad (32)$$

The inputs σ_n , D_n , and s_{n+1} are the stress at the end of the previous timestep, damage at the previous timestep, and starter flaw size (which is a constant); these are all known at the start of the crack growth calculation. This nonlinear equation for l_{n+1} is solved using the TOMS 748 algorithm¹² implementation in the Boost C++ numerical library for each flaw family (or bin).

The default behavior of the updated model uses micro-macro scale consistency to determine the amount of inelastic deformation due to the microcrack growth. Inelastic deformation is allowed in the flow direction associated with granular flow (M , defined in Eq. 50) with a magnitude (λ_D) such that the energy dissipated is equal to the additional surface energy added per unit volume due to micro crack

growth.

$$\Delta\Psi_{\text{micro}} = \pi\gamma_s \sum_k \omega_k ((s_k^{n+1} + l_k^{n+1})^2 - ((s_k^n + l_k^n)^2)) \quad (33)$$

$$\Delta\Psi_{\text{macro}} = \boldsymbol{\sigma} : \Delta\lambda_D \mathbf{M} \quad (34)$$

$$\boldsymbol{\sigma} = \boldsymbol{\sigma}_{\text{tr}} - \mathbb{C} : \Delta\lambda_D \mathbf{M}. \quad (35)$$

The stress at the end of the damage increment depends on the elastic moduli (\mathbb{C}), trial stress ($\boldsymbol{\sigma}_{\text{tr}}$), and the increment in inelastic deformation associated with damage growth ($\Delta\lambda_D \mathbf{M}$). The direction of inelastic deformation (\mathbf{M}) is determined by projecting the trial stress back to the granular flow yield surface. This surface may be much smaller than the current stress causing damage growth. However, the return algorithm for granular flow was designed to handle large trial stresses relative to the yield surface. Equating the microscale energy dissipation ($\Delta\Psi_{\text{micro}}$) with the macroscale dissipation ($\Delta\Psi_{\text{macro}}$) results in a quadratic equation for the magnitude of the increment in granular flow associated with damage growth

$$\Delta\Psi_{\text{micro}} = \boldsymbol{\sigma}_{\text{tr}} : \Delta\lambda_D \mathbf{M} - (\mathbb{C} : \Delta\lambda_D \mathbf{M}) : \Delta\lambda_D \mathbf{M} \quad (36)$$

$$\Delta\lambda_D = \frac{(\boldsymbol{\sigma}_{\text{tr}} : \mathbf{M}) - \sqrt{(\boldsymbol{\sigma}_{\text{tr}} : \mathbf{M})^2 - 4(\mathbf{M} : \mathbb{C} : \mathbf{M}) \Delta\Psi}}{2(\mathbf{M} : \mathbb{C} : \mathbf{M})}. \quad (37)$$

The legacy behavior, where the moduli are reduced with damage growth, is recovered by setting the parameter `GPRefStress`<0. While reasonable for tensile loading within the linear regime, the legacy behavior is questionable under large compressive loads. Particularly, plate impact experiments conducted with a shock-release-reshock loading have suggested that the elastic wave speed does not change in boron carbide after the development of damage under uniaxial strain loading.⁵ This new energy-based behavior introduces stress relaxation that will appear to reduce the bulk modulus in tension and provide bulking in compression.

3.4 Granular Flow

The 2-surface granular flow model implemented in the original version of the Tonge-Ramesh model is particularly inefficient because the intermediate solution for the pressure after the linear Drucker–Prager solve can be unreasonably large. The single surface model avoids this issue, but the multi-stage return algorithm used for

the projection back to the yield surface was not suitable for arbitrarily large strain increments.¹³

3.4.1 Yield Surface

The yield function⁶ is written in terms of the Lode invariants of the stress r , z , and θ . History dependence is addressed by defining 2 history variables that are functions of the inelastic strain rate due to granular flow (ϵ_{GP}). These separate the volumetric component of the inelastic strain ($\epsilon_p^v = \int_0^t \text{tr}(\dot{\epsilon}_{GP}) d\tau$) from the deviatoric component ($\gamma_p = \int_0^t ||\text{dev}[\dot{\epsilon}_{GP}]|| d\tau$). The yield function is similar to the one used in the TR1a model. The differences between this form and the TR1a form are in the Lode angle dependence ($\bar{r}(\theta)$), and the parameter a_3 was removed in favor of placing z_0 inside the exponential. Additionally the changes in the use of the history variables make the form of the model slightly more general.

$$f(r, z, \theta, \gamma_p, \epsilon_p^v) = \frac{1}{2}r^2 - \bar{r}^2(\theta)F_f(z, \gamma_p) |F_f(z, \gamma_p)| F_c(z, \epsilon_p^v) \quad (38)$$

$$F_f(z, \gamma_p) = a_1 - a_1 \exp\left(a_2\sqrt{3}(z - z_0)\right) - a_4\sqrt{3}(z - z_0) \quad (39)$$

$$F_c(z, \epsilon_p^v) = \begin{cases} 1 - \frac{(\kappa(\epsilon_p^v) - \sqrt{3}z)^2}{(\kappa(\epsilon_p^v) - X(\epsilon_p^v))^2} & \text{if } \sqrt{3}z < \kappa \\ 1 & \text{otherwise} \end{cases} \quad (40)$$

$$\mu(\gamma_p) = \mu_1 + (\mu_0 - \mu_1) \exp(-\mu_2\gamma_p) \quad (41)$$

$$z_0(\gamma_p) = z_0^1 + (z_0^0 - z_0^1) \exp(-\mu_2\gamma_p) \quad (42)$$

$$a_2 = \begin{cases} \frac{\mu - a_4}{a_1} & \text{if } a_1 > 0 \\ 0 & \text{otherwise} \end{cases} \quad (43)$$

$$X(\epsilon_p^v) = p_1 \left(p_0 + \frac{1}{2} (\ln(p_3 + p_2\epsilon_p^v) - |\ln(p_3 + p_2\epsilon_p^v)|) \right) \quad (44)$$

$$\kappa(\epsilon_p^v) = p_4 X(\epsilon_p^v). \quad (45)$$

A valid yield surface requires the following:

- $\mu \geq a_4$
- $a_1 \geq 0$, $a_1 = 0$ is only valid if $a_4 > 0$
- $a_4 \geq 0$

- $X < z_0$
- $0 \leq p_4 < 1$
- $p_3 > 0$
- $p_1 > 0$

The yield surface under triaxial compression ($\sigma_1 \leq \sigma_2 = \sigma_3$) is illustrated in Fig. 4. The yield surface parameters used to generate this plot were chosen to illustrate the different features of the model and are not representative of actual material parameters.

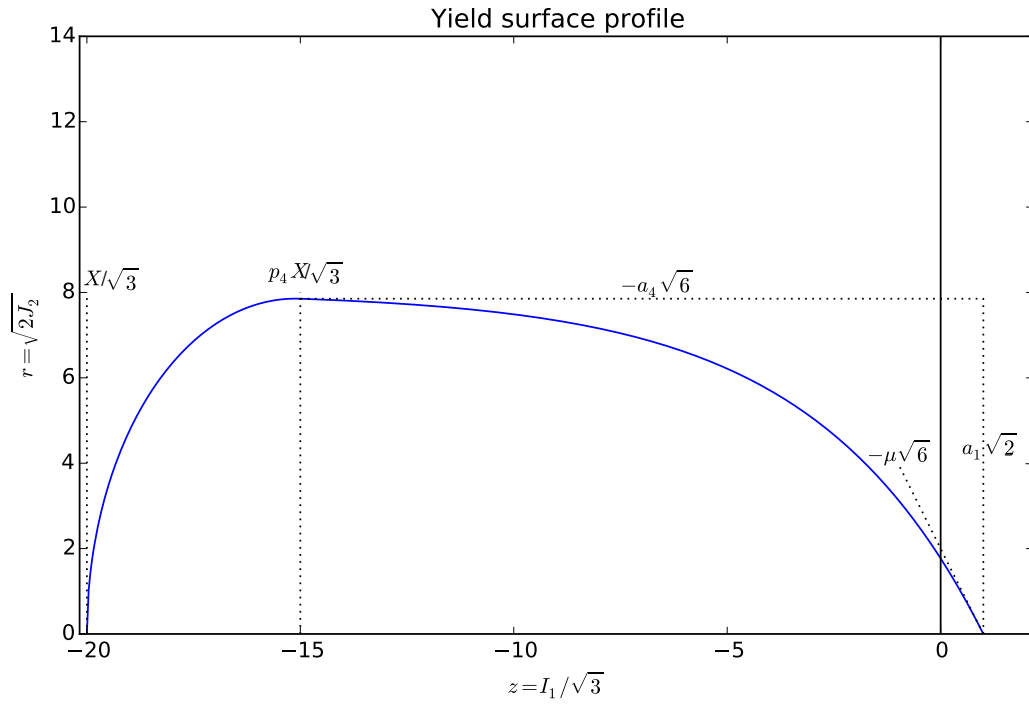


Fig. 4 Meridional profile of the granular material yield surface showing the effect of important input parameters

The Load angle dependence follows a modified Reuleaux profile, which enables an analytic return in the θ direction,¹⁴

$$\bar{b} = \frac{\bar{r}_e^2 - \bar{r}_e + 1}{2\bar{r}_e - 1} \quad (46)$$

$$\bar{a} = \bar{b} - \bar{r}_e \quad (47)$$

$$\xi = \frac{\pi}{6} - \theta - \arcsin\left(\frac{\bar{a} \sin(5\pi/6 + \theta)}{\bar{b}}\right) \quad (48)$$

$$\bar{r}(\theta) = \sqrt{\bar{a}^2 + \bar{b}^2 - 2\bar{a}\bar{b}\cos(\xi)}. \quad (49)$$

Here \bar{r}_e is the ratio of the triaxial tensile strength to the triaxial compressive strength. This ratio must be greater than 0.5 and no more than 1.0. Nonlinear Drucker–Prager behavior is recovered when $\bar{r}_e = 1$. Figure 5 shows the normalized octahedral profile as the parameter \bar{r}_e is changed. There is an edge under triaxial extension.

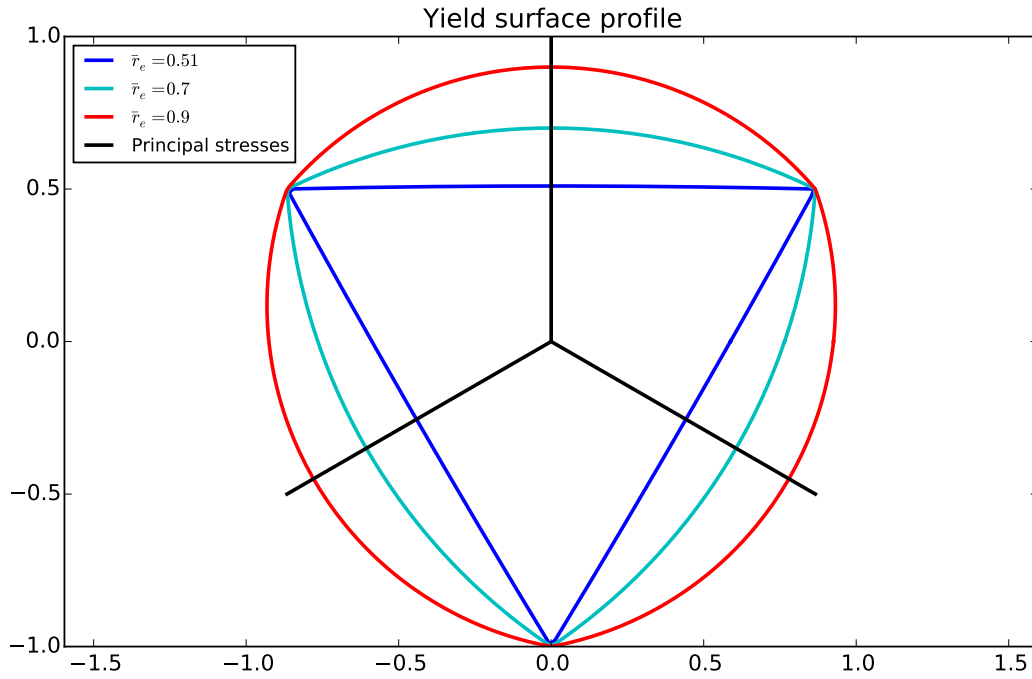


Fig. 5 Normalized octahedral profile of the granular material yield surface showing the effect of the parameter \bar{r}_e

The plastic flow direction is

$$\mathbf{M} = \alpha(\mathbf{N}_{\text{dev}} + \beta\mathbf{N}_{\text{iso}}). \quad (50)$$

Here β is a parameter between 0 and 1 that controls the degree of nonassociativity in the flow direction, \mathbf{N} is the normal to the yield surface (with isotropic component \mathbf{N}_{iso} and deviatoric component \mathbf{N}_{dev}), and α is a normalization to satisfy $\|\mathbf{M}\| = 1$. For associative flow set $\beta = 1$. The edge and vertex cases are addressed by using a closest point projection in an appropriately mapped energy space. This definition of the flow direction (\mathbf{M}) requires an implicit solution of the plasticity return. The algorithm is discussed in Section 3.7.1.

3.4.2 Rate Dependence

The original Tonge-Ramesh material model used a Duvaut–Lions viscoplasticity model with a constant relaxation time τ_{GP} . The linear viscosity model is a reasonable first approximation, but a Bagnold granular gas scaling model^{15,16} is able to incorporate additional physical processes. This scaling relationship arises from a momentum balance when the granular flow is behaving like a gas. When the primary momentum transfer mechanism between particles in the granular flow is brief particle collisions, the shear strain rate $\dot{\gamma}$ scales with the relative particle density $\bar{\rho}$, particle size d , particle coefficient of restitution e , the solid material density ρ_0 , and the shear stress τ

$$\dot{\gamma} \propto \left(\frac{1 - \bar{\rho}^{1/3}}{\bar{\rho}^{1/3}} \right) \left(\frac{1}{d} \right) \sqrt{\frac{6\tau}{e(1+e)\rho_0\pi}}. \quad (51)$$

The model uses this relationship as a guide and assumes a relationship between the inelastic deformation rate (which is not necessarily volume preserving) and the total overstress (which is not necessarily purely deviatoric)

$$\dot{\epsilon} \propto \left(\frac{1 - \bar{\rho}^{1/3}}{\bar{\rho}^{1/3}} \right) \left(\frac{1}{d} \right) \sqrt{\frac{6}{e(1+e)\rho_0\pi}} G \frac{\mathbb{C}^{-1} : (\boldsymbol{\sigma} - \boldsymbol{\sigma}_{qs})}{\sqrt{\|\boldsymbol{\sigma} - \boldsymbol{\sigma}_{qs}\|}}. \quad (52)$$

The particle size (d) and the relative packing density ($\bar{\rho}$) are functions of the history variables

$$d = \left(\sum_{N_{\text{bins}}}^{l_k > 2s_k} \omega_k \right)^{1/3} \quad (53)$$

$$\bar{\rho}^{1/3} = \exp(-\epsilon_v/3). \quad (54)$$

To facilitate writing the constitutive model as a collection of nondimensional terms, we define a reference stress (σ_{ref}), reference relative density $\bar{\rho}_{\text{ref}}$, and reference particle size d_{ref} . From these reference quantities, the coefficient of restitution of the particles during a collision and the material density, a reference strain rate can be computed

$$\dot{\epsilon}_{\text{ref}} = G \left(\sqrt{\frac{6}{e(1+e)\rho_{\text{ref}}\pi}} \right) \left(\frac{1 - \bar{\rho}_{\text{ref}}^{1/3}}{\bar{\rho}_{\text{ref}}^{1/3}} \right) \left(\frac{1}{d_{\text{ref}}} \right) \frac{G^{-1}\sigma_{\text{ref}}}{\sqrt{\sigma_{\text{ref}}}}. \quad (55)$$

Using these reference quantities, the strain rate equation can be written as the product of dimensionless groups

$$\dot{\epsilon} = \dot{\epsilon}_{\text{ref}} \left(\frac{G}{\sigma_{\text{ref}}} \right) \left(\frac{1 - \bar{\rho}^{1/3}}{\bar{\rho}^{1/3}} \frac{\bar{\rho}_{\text{ref}}^{1/3}}{1 - \bar{\rho}_{\text{ref}}^{1/3}} \right) \left(\frac{1}{d} \frac{d_{\text{ref}}}{1} \right) \frac{\mathbb{C}^{-1} : (\boldsymbol{\sigma} - \boldsymbol{\sigma}_{qs})}{\sqrt{\|\boldsymbol{\sigma} - \boldsymbol{\sigma}_{qs}\|/\sigma_{\text{ref}}}}. \quad (56)$$

The Bagnold scaling relationship was derived for granular gasses^{15,16} and breaks down as the relative density of the granular material approaches 1 ($\bar{\rho} \rightarrow 1$) to address this case we only compute the strain rate using a maximum value of $\bar{\rho}_{\text{ref}}$ for $\bar{\rho}$.

It is computationally convenient to write the strain rate sensitivity as a Duvion-Lions viscous relaxation model

$$\dot{\epsilon}_{GP} = \frac{1}{\tau_{GP}} \mathbb{C}^{-1} : (\boldsymbol{\sigma} - \boldsymbol{\sigma}_{qs}) \quad (57)$$

$$\frac{1}{\tau_{GP}} = \left(\frac{G\dot{\epsilon}_{\text{ref}}}{|\sigma_{\text{ref}}|} \right) \left(\frac{(1 - \bar{\rho}^{1/3})\bar{\rho}_{\text{ref}}^{1/3}}{\bar{\rho}^{1/3}(1 - \bar{\rho}_{\text{ref}}^{1/3})} \right) \left(\frac{d_{\text{ref}}}{d} \right) \sqrt{\left(\frac{|\sigma_{\text{ref}}|}{\|\boldsymbol{\sigma} - \boldsymbol{\sigma}_{qs}\|} \right)}. \quad (58)$$

If $\bar{\rho} > \bar{\rho}_{\text{ref}}$, the fraction involving the relative packing density terms is evaluated to 1. The relative packing density scaling can be disabled by setting $\bar{\rho}_{\text{ref}} < 0$ in the input. Similarly, the particle size scaling is disabled by setting $d_{\text{ref}} < 0$ or running the calculation is run without damage growth.

The material model has 3 options for the rate dependence of the granular flow process: rate independent (GPRefStrainRate=0), Bagnold granular gas scaling^{15,16} (GPRefStrainRate>0), and a linear viscosity model (GPRefStrainRate<0).

The linear viscosity model is

$$\frac{1}{\tau_{GP}} = \frac{G|\dot{\epsilon}_{\text{ref}}|}{|\sigma_{\text{ref}}|}. \quad (59)$$

3.5 TR2 Material Model Parameters

The parameters for the TR2 model are summarized in Table 1.

Table 1 Material parameters in TR2 model

Keyword	Symbol	Units	Meaning
MGC0	C_0	L/T	Bulk sound speed
MGGamma0	Γ_0	...	Grüneisen constant
MGS1	s_1	...	Linear term in shock speed relation
MGS2	s_2	...	Quadratic term in shock speed relation
MGS3	s_3	...	Cubic term in shock speed relation
ShearModulus	G	P	Shear modulus
rho_orig	ρ_0	M/L ³	Reference density
FlawDensity	η	1/L ³	Number density of flaws
MinFlawSize	s_{\min}	L	Minimum flaw size in Pareto distribution
MaxFlawSize	s_{\max}	L	Maximum flaw size in Pareto distribution
FlawDistExponent	α	...	Exponent in the Pareto distribution
RandomSeed	...	integer	Seed for randomization
RandomMethod	...	integer	Set randomization method less than 0 to disable
BinBias	Skews flaw binning for methods 6 and 7
FlowStress	τ_0	P	Initial J2 flow stress (set less than 0 to disable)
HardeningModulus	H	P	Hardening modulus for J2 flow
J2RelaxationTime		T	Viscous timescale for J2 flow
KIc	K_{IC}	PL ^{1/2}	Critical stress intensity for crack growth
FlawFriction	μ	...	Friction across the crack faces
FlawAngle	ϕ	radians	Flaw orientation
FlawGrowthExponent	γ_c	...	Exponent for crack growth law
FlawGrowthVel	v_m	L/T	Maximum crack speed
CriticalDamage	D_c	...	Damage to activate granular flow
GPreRefStrainRate	$\dot{\epsilon}_{\text{ref}}$	1/T	Granular flow reference strain rate
GPreRefStress	σ_{ref}	P	Granular flow reference stress
GPreRefRhoBar	$\bar{\rho}_{\text{ref}}$...	Reference packing density
GPreRefSize	d_{ref}	L	Reference particle size
GFMSm0	μ_0	...	Initial low pressure slope
GFMSm1	μ_1	...	Final low pressure slope
GFMSm2	μ_2	...	Slope change rate with strain
GFMSp0	p_0	...	Crush curve parameter
GFMSp1	p_1	P	Crush curve parameter
GFMSp2	p_2	...	Crush curve parameter
GFMSp3	p_3	...	Crush curve parameter
GFMSp4	p_4	...	Shear pressure coupling for pore collapse
GFMSa1	a_1	...	Extrapolation of the a_4 slope to z_0
GFMSz00	z_0^0	P	Initial granular hydrostatic tensile strength
GFMSz01	z_0^1	P	Final granular hydrostatic tensile strength
GFMSa4	a_4	P	High pressure slope
GFMSBeta	β	...	nonassociativity for granular flow
GFMSPsi	\bar{r}_e	...	Strength reduction ratio for triaxial extension

In this new model the parameters v_m , $\dot{\epsilon}_{\text{ref}}$, σ_{ref} , $\bar{\rho}_{\text{ref}}$, and d_{ref} are new. Many redundant parameters and switches were removed. The form of the yield surface softening is different between TR1a and TR2; however, for a granular flow response that is independent of γ_p , the yield surfaces can be made similar

$$\mu^{\text{TR2}} = a_2^{\text{TR1a}} a_3^{\text{TR1a}} + \mu^{\text{TR1a}} \quad (60)$$

$$a_4^{\text{TR2}} = \mu^{\text{TR1a}} \quad (61)$$

$$a_1^{\text{TR2}} = \begin{cases} a_1^{\text{TR1a}} & \text{if } a_2^{\text{TR1a}} \neq 0 \\ 0 & \text{otherwise} \end{cases} \quad (62)$$

$$a_1^{\text{TR1a}} = a_3^{\text{TR1a}} \exp(a_2^{\text{TR1a}} z_0^{\text{TR2}} \sqrt{3}) + \mu^{\text{TR1a}} z_0^{\text{TR2}} \sqrt{3}. \quad (63)$$

3.6 TR2 History Variables

In addition to removing redundant parameters and switches, the new model uses fewer history variables. The history variables that are specific to this material model are listed in Table 2. The subscripted flaw family information is repeated for the number of flaw families that are included in the problem. The total number of history variables is 7 plus 3 multiplied by the number of flaw families.

Table 2 Model specific history variables

Name	Symbol	Units	Meaning
BulkModulus	K	P	Bulk modulus
ShearModulus	G	P	Shear modulus
damage	D	...	Damage variable
plasticStrain	ϵ_p	...	Plastic strain due to volume preserving plasticity
plasticEnergy	...	P	Energy absorbed by volume preserving plasticity
epsv	ϵ_p^v	...	Inelastic volume strain due to granular flow
gam	γ_p	...	Inelastic deviatoric strain due to granular flow
flawNumber_k	ω_k	$1/L^3$	Number density of flaws for bin k
starterFlawSize_k	s_k	L	Representative flaw size for bin k
wingLength_k	l_k	L	Wing crack length for bin k

In addition to the model specific history variables listed in Table 2, the material model tracks the stored strain energy per unit mass (e_{elas}) and the dissipated energy per unit mass (e_{plas}). These are integrated using a first-order accurate scheme

$$\Delta e_{\text{tot}} = \frac{\boldsymbol{\sigma}_{n+1} : \Delta \boldsymbol{\epsilon}}{\rho} \quad (64)$$

$$\Delta \boldsymbol{\sigma} = \boldsymbol{\sigma}_{n+1} - \boldsymbol{\sigma}_n \quad (65)$$

$$\Delta \boldsymbol{\epsilon}_e = \frac{\Delta \boldsymbol{\sigma}_{\text{iso}}}{3K} + \frac{\Delta \boldsymbol{\sigma}_{\text{dev}}}{2G} \quad (66)$$

$$\Delta e_{\text{elas}} = \frac{\boldsymbol{\sigma}_{n+1} : \Delta \boldsymbol{\epsilon}_e}{\rho} \quad (67)$$

$$\Delta e_{\text{plas}} = \Delta e_{\text{tot}} - \Delta e_{\text{elas}}. \quad (68)$$

Here $\boldsymbol{\sigma}_n$ is the stress entering the material subroutine and $\Delta \boldsymbol{\epsilon}$ is the increment in strain. The stored strain energy per unit mass is stored in the `sse` history variable, and the dissipated energy per unit mass is stored in the `spd` history variable.

3.7 Numerical Implementation

This material model is implemented as an Abaqus User Material and assumes that the stress and strain increment coming into the material model interface accounts for objectivity requirements through the use of an objective rate or the an “unrotated” configuration. Either approach can be used because there are no tensor internal state variables in the model.

Since rotations are not considered in the constitutive model and there are no internal tensor variables, all stress or strain tensors are symmetric second-order tensors allowing significant improvements in associated tensor operations. In particular, specialized formulas are used to determine the eigen values, eigen projectors,¹⁷ and inverse when needed.

The damage growth calculation uses the stress at the beginning of the timestep. The volume preserving plasticity mechanism is computed first using a radial return algorithm. The output of the volume preserving plasticity calculation used as the trial stress for the granular flow calculation when granular flow is active. The granular flow algorithm is more involved due to the pressure and possible Lode angle dependence. The numerical approach is described in the following section.

3.7.1 Rate Independent Projection

The modified Reuleaux profile¹⁴ has a hydrostatic tensile vertex, edges in triaxial compression, and the remaining surfaces are smooth nonplanar surfaces. The input

to the return algorithm is a trial stress (σ_{tr}), the Poisson's ratio (ν), the parameters describing the current location of the yield surface ($a_1, a_2, a_4, \bar{r}_e, X$, and κ), and the parameter determining the degree of nonassociativity in the plastic flow direction (β). From the trial stress, the Lode coordinates ($z_{\text{tr}}, r_{\text{tr}}$, and θ_{tr}) and eigen projectors (P_1, P_2 , and P_3) are calculated. After this, the return algorithm checks the hydrostatic tensile vertex, then attempts returning to the smooth nonplanar surface. If the nonplanar return causes the stress to change sextants ($\theta < -\frac{\pi}{6}$), then the return should be to the triaxial compression edge.

The modified Reulaux profile reduces the number of unknowns in the nonplanar stress return to only the hydrostatic pressure

$$\zeta = \frac{1}{\beta} \sqrt{\left(\frac{1-2\nu}{1+\nu} \right)} \quad (69)$$

$$r_c(z) = \begin{cases} F_f(z) \sqrt{2F_c(z)} & \text{if } F_c > 0 \text{ and } F_f > 0 \\ 0 & \text{otherwise} \end{cases} \quad (70)$$

$$b_T(z) = \sqrt{(\bar{a}r_c(z))^2 + r_{\text{tr}}^2 - 2\bar{a}r_c(z)r_{\text{tr}}\cos(5\pi/6 + \theta_{\text{tr}})} \quad (71)$$

$$b(z) = \bar{b}r_c(z) \quad (72)$$

$$L^2(z) = (b_T(z) - b(z))^2 + (\zeta z - \zeta z_{\text{tr}})^2. \quad (73)$$

The closest point return in the energy norm is z_{CP} where z_{CP} minimizes L^2 .^{14,18} The nonlinear minimization problem is solved using Brent's algorithm¹⁹ implemented in the Boost C++ library. After computing z_{CP} , the radial coordinate (r_{CP}) and Lode angle θ_{CP} are given by

$$\xi_{\text{CP}} = \arcsin \left(\frac{r_{\text{tr}} \sin(5\pi/6 + \theta_{\text{tr}})}{b_T(z_{\text{CP}})} \right) \quad (74)$$

$$\bar{r}_{\text{CP}} = \sqrt{\bar{a}^2 + \bar{b}^2 - 2\bar{a}\bar{b}\cos(\xi)} \quad (75)$$

$$r_{\text{CP}} = \bar{r}_{\text{CP}}r_c(z_{\text{CP}}) \quad (76)$$

$$\theta_{\text{CP}} = \arccos \left(\frac{\bar{a}^2 + \bar{r}_{\text{CP}}^2 - \bar{b}^2}{2\bar{a}r_{\text{CP}}} \right) - \frac{5\pi}{6}. \quad (77)$$

If the computed Lode angle for this return is outside of the original sextant ($\theta_{\text{CP}} < -\pi/6$), then the return will be to the triaxial compression edge ($\theta_{\text{CP}} = -\pi/6$). The

minimization problem for this return case is

$$L_e^2 = \left(r_{\text{tr}} \cos \left(\frac{\pi}{6} + \theta_{\text{tr}} \right) - r_c(z) \right)^2 + (\zeta z - \zeta z_{\text{tr}})^2. \quad (78)$$

Once the Lode coordinates are computed, the return stress is reconstructed from the principal stresses and the eigen projectors of the trial stress (\mathbf{P}_1 , \mathbf{P}_2 , and \mathbf{P}_3)

$$\sigma_1 = \frac{z_{\text{CP}}}{\sqrt{3}} + \frac{r_{\text{CP}}}{\sqrt{2}} \left(\frac{\sin(\theta_{\text{CP}})}{\sqrt{3}} - \cos(\theta_{\text{CP}}) \right) \quad (79)$$

$$\sigma_2 = \frac{z_{\text{CP}}}{\sqrt{3}} - r_{\text{CP}} \sin(\theta_{\text{CP}}) \sqrt{\frac{2}{3}} \quad (80)$$

$$\sigma_3 = \frac{z_{\text{CP}}}{\sqrt{3}} + \frac{r_{\text{CP}}}{\sqrt{2}} \left(\frac{\sin(\theta_{\text{CP}})}{\sqrt{3}} + \cos(\theta_{\text{CP}}) \right) \quad (81)$$

$$\boldsymbol{\sigma}_{\text{qs}} = \sigma_1 \mathbf{P}_1 + \sigma_2 \mathbf{P}_2 + \sigma_3 \mathbf{P}_3. \quad (82)$$

This return does not account for the evolution of the internal state variables during the timestep. The nonhardening return algorithm can be used as the basis for a consistent hardening solution.¹⁸ At the end of a timestep using a consistent algorithm, the stress lies on the yield surface that has been updated based on the strain increment during the timestep

$$f(\boldsymbol{\sigma}_{n+1}, \epsilon_{vn+1}^p, \gamma_{pn+1}) = 0. \quad (83)$$

To generate a consistent hardening solution we iteratively solve

$$y(\eta) = \delta \epsilon_v^p - \eta \delta \epsilon_{v0}^p = 0. \quad (84)$$

Here $\delta \epsilon_{v0}^p$ is the increment in ϵ_v^p computed using the nonhardening return algorithm and ϵ_{vn}^p . The quantity $\delta \epsilon_v^p$ is computed from the nonhardening return algorithm after updating the history variables according to

$$\epsilon_v^p = \epsilon_{vn}^p + \eta \delta \epsilon_{v0}^p. \quad (85)$$

For a hardening process, the solution to Eq. 84 is bounded between 0 and 1. A known bounding range for the solution enables solution algorithms that are guaranteed to converge.¹⁸ We do not try to generate a consistent solution that accounts for possible softening due to evolving γ_p .

Figure 6 illustrates the difference in convergence behavior when the consistent return is used. These simulations are for a single element that starts with an inelastic volume strain of 0.6, and then the porosity is compressed out of the material. There is minimal error in the pressure solution for the consistent algorithm even with a strain increment of 0.1. The faster algorithm that does not account for the evolution of the yield surface during the timestep does not seem to converge until a strain increment of 0.001. Both algorithms converge to the same pressure-volume response at a strain increment of 0.001 as shown in Fig. 7.

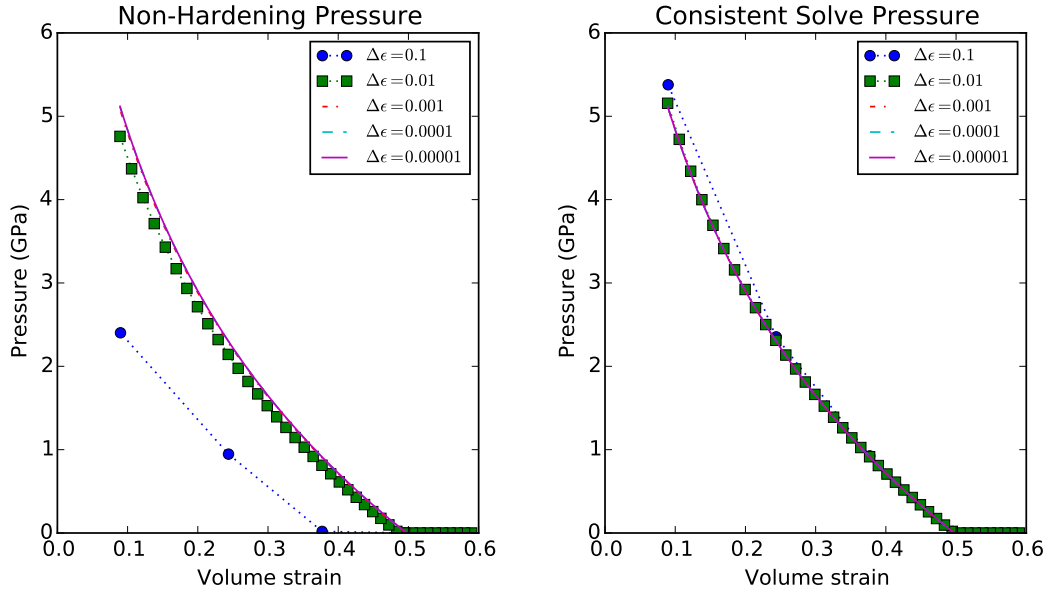


Fig. 6 Comparison of single element uniaxial strain compression simulations from an initially distended state showing the effect of strain increment size

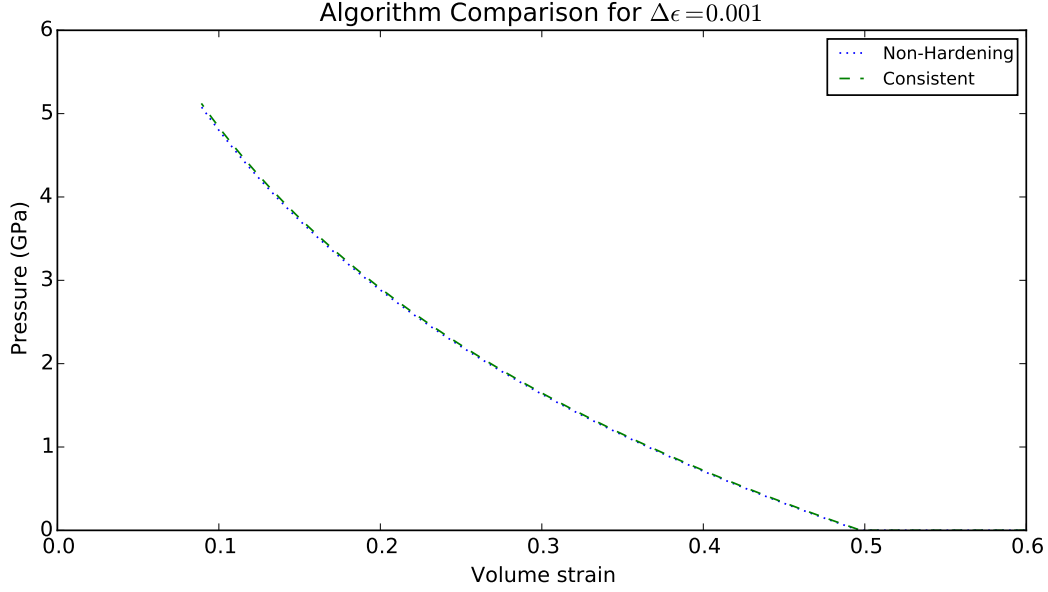


Fig. 7 Pressure-volume response for an initially distended material for uniaxial strain compression with a strain increment of 0.001 for the consistent algorithm and the faster nonhardening algorithm

3.7.2 Rate Dependence

The numerical implementation of the granular flow viscoplasticity model relies on the ability to project an arbitrary trial stress (σ_{tr}) onto the quasi-static yield surface (providing the value for σ_{qs}). Once the projection onto the quasi-static yield surface is defined, the stress at the end of the timestep is

$$\sigma_{n+1} = \frac{\sigma_{tr} + \left(\frac{\Delta t}{\tau_{GP}}\right) \sigma_{qs}}{1 + \frac{\Delta t}{\tau_{GP}}}. \quad (86)$$

This procedure²⁰ to update the stress only requires tracking the current stress as a history variable and is more robust with respect to advection errors (provided that σ_{qs} can be computed reliably) than the algorithm that explicitly tracked σ_{qs} as an extra set of history variables. When using the Bagnold-type granular flow rate, the relaxation time τ_{GP} is approximated using the trial stress as

$$\frac{1}{\tau_{GP}} = \left(\frac{G\dot{\epsilon}_{ref}}{|\sigma_{ref}|}\right) \left(\frac{(1 - \bar{\rho}^{\frac{1}{3}})\bar{\rho}_{ref}^{\frac{1}{3}}}{\bar{\rho}^{\frac{1}{3}}(1 - \bar{\rho}_{ref}^{\frac{1}{3}})}\right) \left(\frac{d_{ref}}{d}\right) \sqrt{\left(\frac{|\sigma_{ref}|}{\|\sigma_{tr} - \sigma_{qs}\|}\right)}. \quad (87)$$

This approximation over estimates the quantity $\|\sigma - \sigma_{qs}\|$ by a factor of $\sqrt{1 + \Delta t / \tau_{GP}}$ to avoid solving a quintic equation numerically. The extra cost of numerically solving the quintic is not justified because the backward Euler stress update algorithm is only first-order accurate.²⁰ Using the trial stress in the calculation instead of the stress from the previous timestep prevents division by zero. For global timesteps that poorly resolve the granular flow timescale τ_{GP} , this algorithm will overestimate the rate of stress relaxation. However, for a decaying function, like the overstress in Eq. 86, the backward Euler update overestimates the updated function value. The updated stress will be outside the yield surface at the end of the timestep avoiding saw tooth behavior caused by over estimating the increment in plastic strain.

3.8 Timing Results

The speed of the improved model was measured by simulating a cube of material subjected to simple shear deformation. The cube was meshed with 1,000 elements (10 elements per side) and the simulation was run for 1,000 timesteps with all displacement degrees of freedom specified. This test compared 3 different material models: the original Tonge-Ramesh implementation with a 2-surface description of the dilatation and compaction surfaces, the single-surface implementation with the multistage return algorithm, and the improved-single-surface model. All implementations were compiled without optimizations. The TR1 model took 40.2 μs /zone/cycle to complete the simulation. The TR1a model took 16.8 μs /zone/cycle, and the improved TR2 model took 4.0 μs /zone/cycle when the consistent solve was used and 2.3 μs /zone/cycle when it was not. These results indicate that the improved model is 5–10 times faster than the original implementation. The timing results are summarized in Table 3. For problems that are dominated by the granular flow part of the calculation, the TR2 model is significantly faster.

Table 3 Summary of model evaluation times for 1,000 elements simulated for 1,000 timesteps

Model	Total model evaluation time (s)
TR1	165
TR1a	17.6
TR2	4.40
TR2 with consistency correction	4.70

The basic single-surface return algorithm in the TR2 model seems to be sufficient for most cases and is faster than using a consistent solution. The uniaxial strain compaction problem used to demonstrate the difference between the faster and the consistent solution is expected to be a worst case. This model is intended to solve problems where the intact material fragments, then porosity is introduced. In these types of loading there will be some re-compression of the material, but it is not expected to dominate the problem.

4. Model Evaluation Methods

4.1 Geometry from Prior Experiments

There are experimental data from 2 research groups on penetration of confined boron carbide by high-density, long-rod projectiles.^{21,22} Based on these prior experiments, the following 3 experimental geometries were identified to test the performance of the material model for impact velocities from 1,000 to 5,000 m/s:

- 1) Boron carbide cylinder 19 mm in diameter and 39.6 mm long encased in 4 mm of steel on the top, sides, and bottom. There was a 0.07-mm interference fit between the confinement and the boron carbide.
- 2) Boron carbide cylinder 19 mm in diameter and 39.6 mm long encased in 1 mm of steel on the sides with 4 mm on the top and bottom. There was a 0.07-mm interference fit between the confinement and the boron carbide.
- 3) Boron carbide cylinder 16 mm in diameter and 50 mm long encased in a 1.59-mm-thick Ti6–Al4 sleeve with a 3.175-mm top plate and 12.7-mm bottom plate. The confining sleeve had a slip fit with the target cylinder.

Geometries 1 and 2 used a 2-mm-diameter tungsten rod that was 150 mm long. Geometry 3 used a 11.43-mm-long tungsten rod that was 0.762 mm in diameter.

4.2 Simulation Mesh

The Lagrangian mesh for geometry 1 is shown in Fig. 8. The mesh for geometry 2 is nearly identical, except elements are removed from the outer circumference of the cylinder to reduce the wall thickness. There are 2 cells across the projectile radius. In these Lagrangian simulations, distorted elements were converted into SPH particles according to history variables that would indicate sufficient loss of

material strength. For steel or tungsten elements, the conversion occurred after the equivalent plastic strain in the element exceeded 1.0. Within the ceramic material, elements were converted once the inelastic shear strain (γ_p) exceeded 0.1.

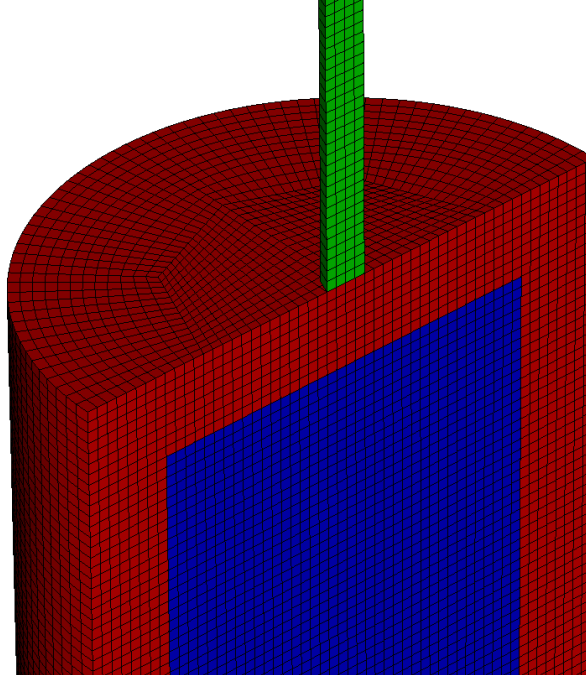


Fig. 8 Slice view of the initial Lagrangian mesh used for the geometry 1 penetration simulations

The initial mesh for the Eulerian simulations of geometry 1 is shown in Fig. 9. The projectile is better resolved with 4 elements across the projectile radius. This mesh attempts to balance limited void material with providing sufficient space for motion of the target after impact.

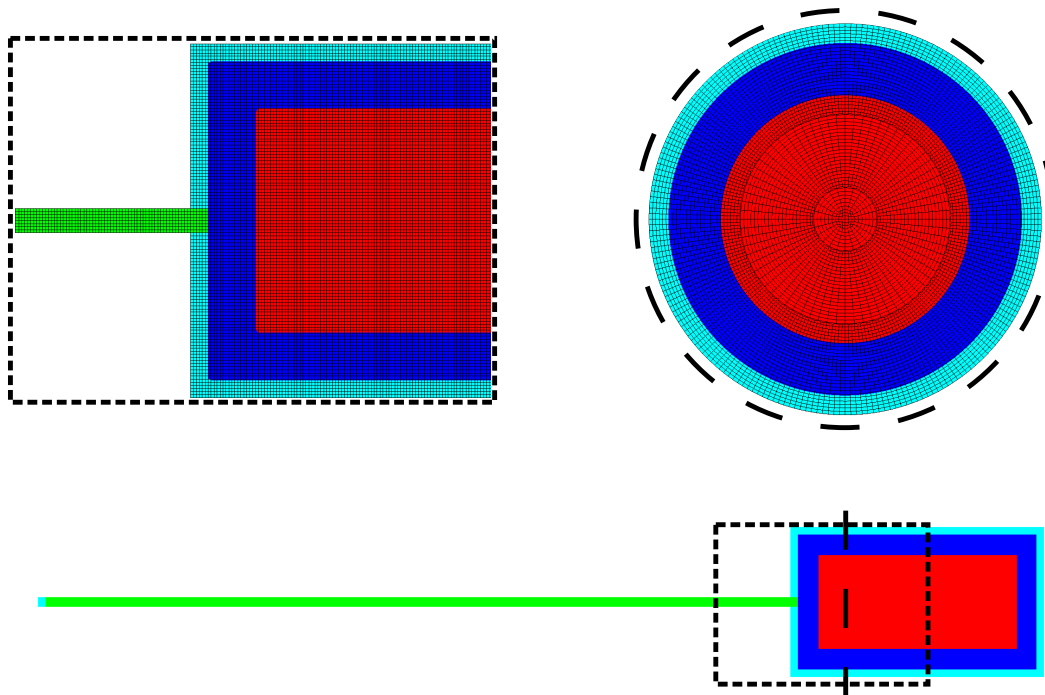


Fig. 9 Representative mesh used for the Eulerian simulations of geometry 1 using 4 elements across the rod radius

The Lagrangian mesh for geometry 3 is shown in Fig. 10. There are 2 cells across the projectile radius. Similar particle conversion rules were used for this set of simulations as for geometries 1 and 2. The short rod and large impact velocity result in conversion of the projectile material into SPH particles very soon after the impact event occurs. The primary purpose of this series of 3 simulations is to test the material model at the limits of its region of applicability.

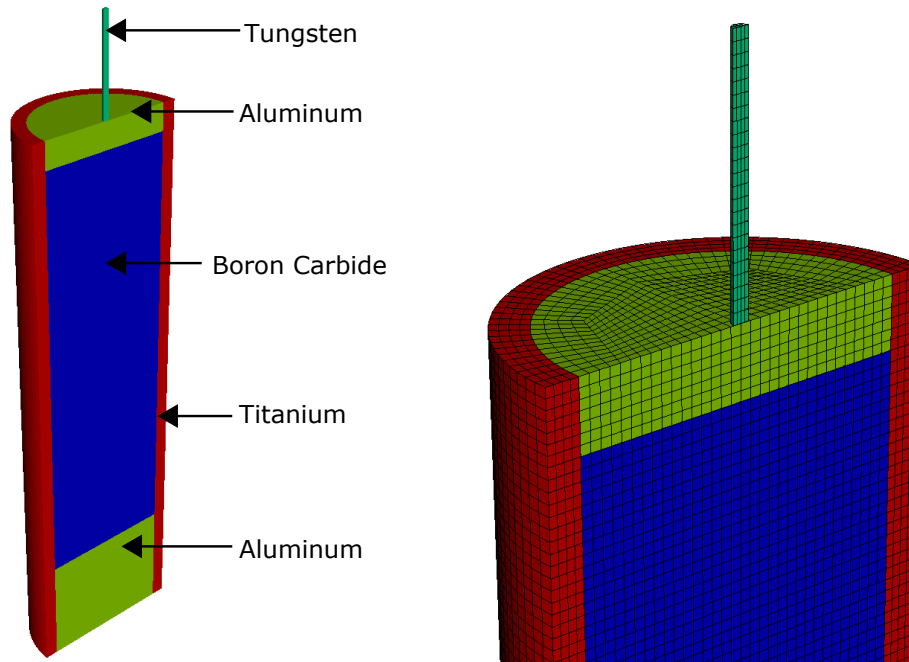


Fig. 10 Cut view of the initial mesh used for Lagrangian simulations of geometry 3

4.3 Material Parameters

The baseline material parameters for boron carbide are taken from the original application of this model to boron carbide.² This set of material parameters does not allow for volume preserving inelastic deformation prior to full damage development ($D \geq 0.125$) and does not limit the strength of the fully damaged material when sufficient pressure is applied. Because the model only allows Drucker–Prager plasticity with pore compaction, at very high pressures, the failed ceramic can sustain unreasonably large deviatoric stresses. These baseline material parameters are listed in the TR1 column of Table 4. To demonstrate sensitivity of the results to the damaged material model, a second set of material parameters were defined based on the JHB parameters for damaged boron carbide (set B).²³ These parameters are listed in column TR1a in Table 4. Simulations using the TR2 model used parameters that were equivalent to the TR1a parameters.

Table 4 Material parameters used in TR1 and TR1a model evaluation

Parameter name	TR1	TR1a	Parameter name	TR1	TR1a
useDamage	1.000e+00	1.000e+00	usePlasticity	0.000e+00	1.000e+00
useGranularPlasticity	1.000e+00	1.000e+00	useOldStress	1.000e+00	1.000e+00
artificialViscosity	0.000e+00	0.000e+00	artificialViscousHeating	0.000e+00	0.000e+00
BulkModulus	2.334e+11	2.334e+11	ShearModulus	1.970e+11	1.970e+11
rho_orig	2.520e+03	2.520e+03	FlowStress	N/A	10.206e+9
HardeningModulus	N/A	0.0	InitialPlasticStrain	N/A	0.000e+00
J2RelaxationTime	N/A	0.000e+00	NumCrackFamilies	2.500e+01	2.500e+01
FlawDensity	2.200e+13	2.200e+13	FlawDistType	Pareto (2)	Pareto (2)
MinFlawSize	1.000e-06	1.000e-06	MaxFlawSize	2.500e-05	2.500e-05
FlawDistExponent	2.600e+00	2.600e+00	RandomizeFlawDist	1.000e+00	1.000e+00
RandomSeed	3.000e+00	3.000e+00	RandomizeMethod	7.000e+00	7.000e+00
BinBias	-2.000e+00	-2.000e+00	KIc	2.500e+06	2.500e+06
FlawFriction	6.000e-01	6.000e-01	FlawAngle	1.044e+00	1.044e+00
FlawGrowthExponent	1.000e+00	1.000e+00	FlawGrowthAlpha	5.000e+00	5.000e+00
CriticalDamage	1.250e-01	1.250e-01	MaxDamage	1.260e-01	1.260e-01
MicroMechPlaneStrain	1.000e+00	1.000e+00	IncInitDamage	1.000e+00	1.000e+00
DoFlawInteraction	1.000e+00	1.000e+00	GPTimeConst	7.000e-09	0.000e+00
JLoc	2.000e+00	2.000e+00	GPGranularSlope	8.000e-01	N/A
GPCohesion	3.000e+06	N/A	GPYieldSurfType	1.000e+00	N/A
GPPc	1.000e+10	N/A	GPJref	2.000e+00	N/A
GPPref	1.000e+08	N/A	GPSurfaceType	0.000e+00	1.000e+00
AbsToll	N/A	1.0e-12	RelToll	N/A	1.0e-08
MaxIter	N/A	20	MaxLevels	N/A	1
GFMSm0	N/A	0.001	GFMSm1	N/A	0.001
GFMSm2	N/A	0.000e+00	GFMSp0	N/A	-1.000e-02
GFMSp1	N/A	1.000e+10	GFMSp2	N/A	1.429e+00
GFMSp3	N/A	5.000e-03	GFMSp4	N/A	7.500e-01
GFMSa1	N/A	288.7e6	GFMSa2	N/A	1.278e-9
GFMSa3	N/A	288.7e6	GFMSBeta	N/A	1.0
GFMSPsi	N/A	1.0	GFMSJ3Type	N/A	0
MGC0	9.600e+03	9.600e+03	MGGamma0	1.280e+00	1.280e+00
MGS1	9.140e-01	9.140e-01	MGS2	0.000e+00	0.000e+00
MGS3	0.000e+00	0.000e+00	MGCv	9.620e+02	9.620e+02
MGTheta_0	2.940e+02	2.940e+02			

For geometry 1 and 2, the projectile and confinement were modeled using a Johnson–Cook plasticity and failure model with the parameters taken from the experimental paper.²² The metals in simulations of geometry 3 were also modeled using a Johnson–Cook plasticity and failure model. The tungsten parameters were adapted from the parameters for geometries 1 and 2 by scaling the density. The other metals were modeled using library parameters.²⁴

5. Results

The majority of the simulations with the baseline material model ran to completion when used with element conversion to SPH particles. The baseline material model ran in Eulerian mode, but a convergence failure while inverting the Mie–Grüneisen equation of state halted the simulation after only 1 μs . The Eulerian run at 1,480 m/s using the TR1a material parameter set ran to 57 μs before crashing due to a “Q-Stop” error. These errors are generally a symptom of some other mesh tangling or mixed zone issue. The log file from this run showed an invalid deformation gradient (\mathbf{F}) in the cell that caused the fatal error. The TR2 version of the model discussed in Section 3 ran the problem to completion. The geometry 3 problems ran to completion for all impact velocities up to 4,500 m/s. The results of the simulations are presented in Table 5 with the corresponding depth of penetration reported in the experimental papers.^{21,22} The material locations at the end of the Lagrangian simulations of geometries 1 and 2 are shown in Fig. 11. The final material locations for the Lagrangian simulations of geometry 3 are shown in Fig. 12.

Table 5 Summary of simulation results

Geometry	Velocity (m/s)	Material model	Simulation type	Sim DOP (mm)	End time (μs)	Exp DOP (mm)
1	1,427	TR1	Lagrange	0	35	6
1	1,427	TR1a	Lagrange	6.9	58	6
1	1,480	TR1	Lagrange	0	60	20
1	1,480	TR1a	Lagrange	7.9	60	20
1	1,480	TR1	Euler	0	1	20
1	1,480	TR1a	Euler	39.2	57	20
1	1,480	TR2	Euler	35.3	60	20
2	1,517	TR1	Lagrange	6.2	60	35
2	2,601	TR1	Lagrange	15.0	25	35
3	1,500	TR1	Lagrange	0	60	11
3	3,000	TR1	Lagrange	2.3	60	22
3	4,500	TR1	Lagrange	4.0	60	26

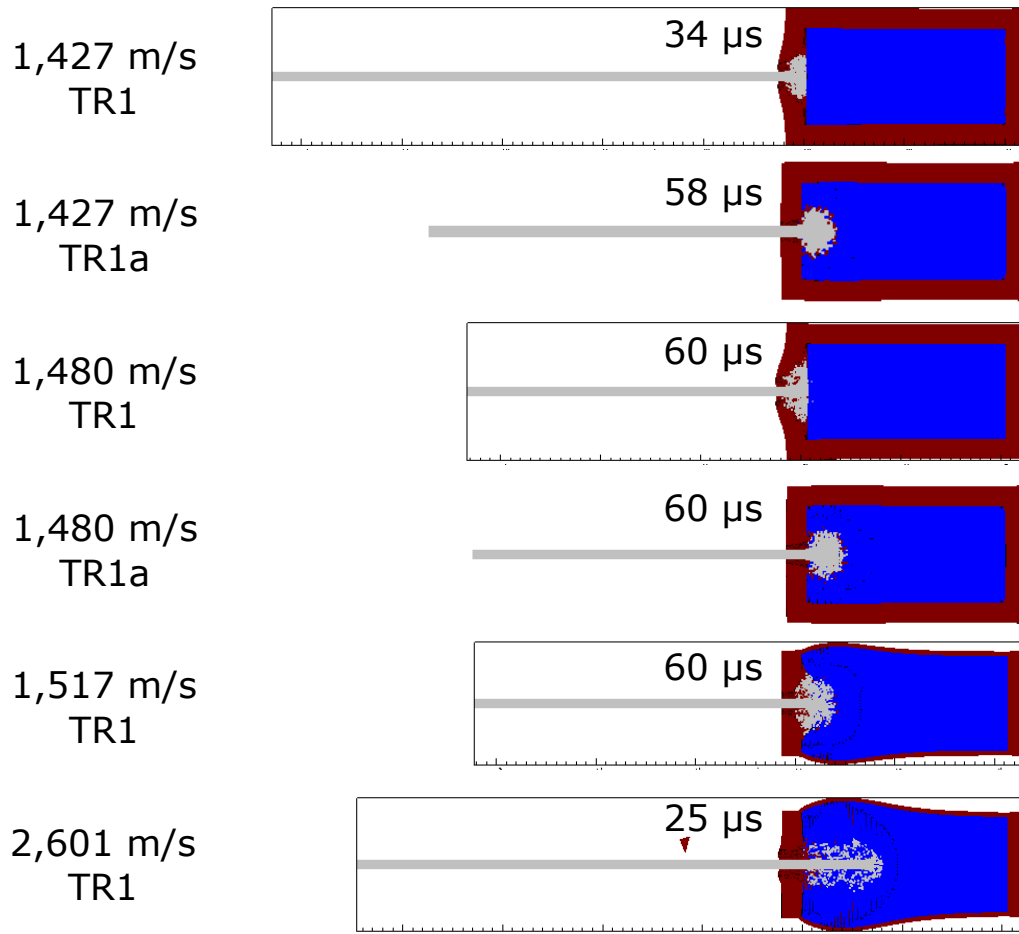


Fig. 11 Comparison of simulation results for the Lagrangian simulations of geometries 1 and 2 at the end of the simulation

For geometry 1, simulations were run using both the TR1 and the TR1a material parameter sets for the 1,427- and 1,480-m/s impact velocities. Experimentally, a dwell to penetration transition was observed between these 2 velocities.²² When using the baseline material parameters, there is interface defeat at both of these velocities; however, in calculations using the TR1a material parameter set, there is 6.9 mm of penetration for the 1,427-m/s impact and 7.9 mm for the 1,480-m/s impact. When the numerical technique is changed from a Lagrangian mesh with conversion to SPH particles to a pure Eulerian formulation, the penetration for the 1,480-m/s impact increases to 39.2 mm. One should not observe such a large difference in the simulation results when the numerical technique is changed. Treatment of failure and strongly history dependent materials within computational frameworks that can

simultaneously handle arbitrarily large shear deformations is an ongoing research area. The meshes used for these simulations are likely too coarse to accurately capture the failure and localization processes in either the Lagrangian or Eulerian simulations. However, the goal of this report was to document that the TR1 model and TR1a model could be run in ALE3D and that a modified model more suitable for large simulations with advection had been created. Understanding the reason for the discrepancy between the Lagrangian and Eulerian approaches is a subject for a different report. Similarly, the material parameters used for this study were chosen for consistency, not to provide the best fit to the experimental observations.

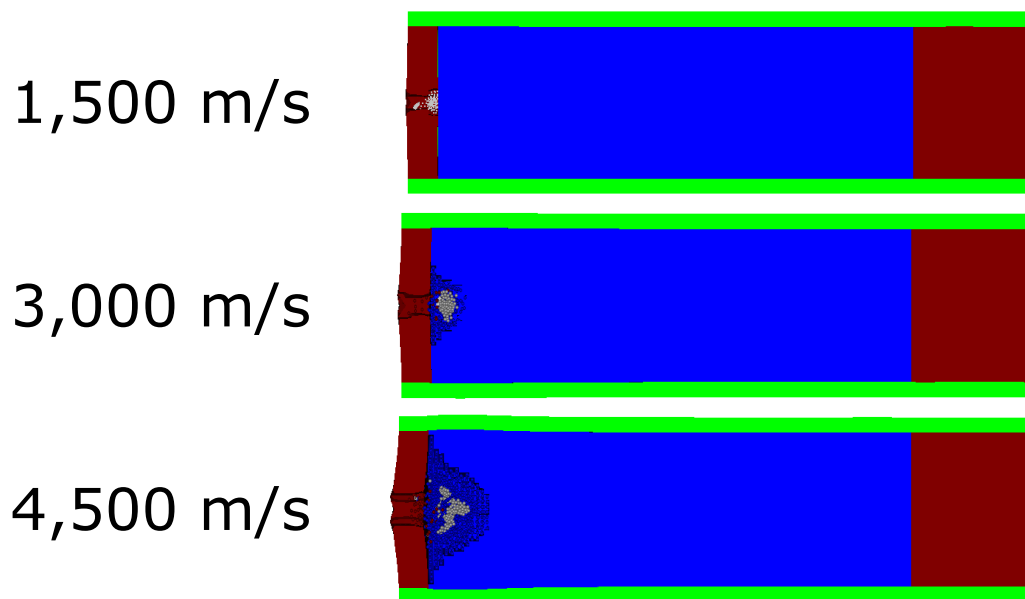


Fig. 12 Comparison of simulation results for the geometry 3 long rod impact geometry 60 μ s after impact

Geometry 3 was only run using the TR1 model parameters in Lagrangian mode with conversion to SPH particles. The purpose of the simulation was to demonstrate that the model would run at impact velocities up to 4,500 m/s. As shown in Fig. 12, the simulations ran to completion at 60 μ s. In the 1,500-m/s simulation there was interface defeat. The 3,000- and 4,500-m/s simulations showed some penetration into the boron carbide but much less than the experimentally observed penetration.

The results of the Eulerian simulations of the 1,480-m/s impact using geometry 1 are shown in Fig. 13. To obtain the reported results for the Eulerian simula-

tions using the TR1a model, the error checking was disabled and the rate dependent granular flow was disabled and replaced with rate independent granular flow. These limitations are addressed in Section 3. Both the TR1a and the TR2 model without rate dependence in the granular flow provide similar results. Introducing rate dependence into the granular flow decreases the amount of penetration. The TR1a model could not be run in Eulerian mode with the rate dependence because the results were severely corrupted by advection errors. The TR2 model discussed in Section 3 is significantly more robust and does not have the same limitations. The Eulerian simulation results show a significantly narrower penetration channel than the Lagrangian simulations with conversion to SPH particles. Flash X-ray images taken during the experiment show a penetration channel that is more consistent with the Eulerian simulations than the Lagrangian simulations, but the reason for the better agreement is unclear. Eulerian simulations using both the consistent and the faster version of the TR2 model produce similar results. Simulations using a finer mesh were also run for the Eulerian case and produced similar results. A mesh convergence study using the Lagrangian simulations with SPH conversion was not performed. The SPH conversion algorithm proved to be very computationally expensive, and the convergence study was not justified based on the SwRI work demonstrating that the TR1 parameter fit may not be reasonable for impact problems involving deep penetration.

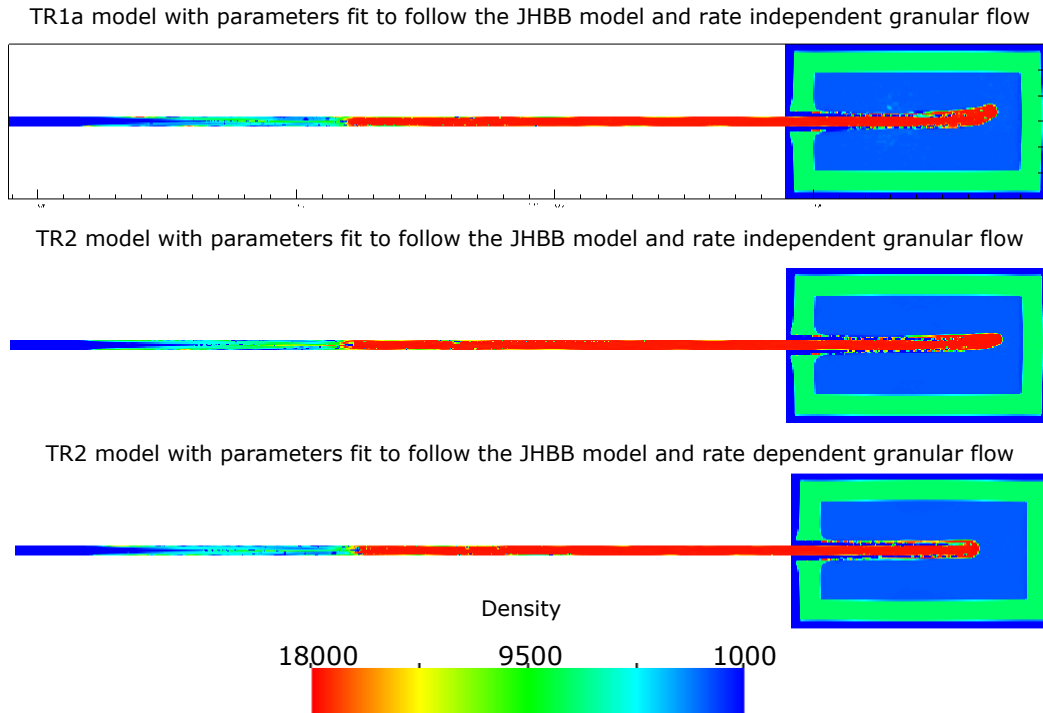


Fig. 13 Comparison of simulation results for the Eulerian simulations of the geometry 1 long rod impact problem using the TR1a and TR2 models with material parameters fit to the JHB set B boron carbide model and an initial impact velocity of 1,480 m/s 50 μ s into the simulation

6. Discussion

These simulations demonstrate that the Tonge-Ramesh material model is implemented in ALE3D and can be used to simulate complex penetration problems up to 4,500 m/s. As discussed by Holmquist et al.,⁴ the TR1 model is relatively robust, but the efficiency could be improved. The default model parameters do not predict the correct dwell to penetration transition. The strength of the damaged material is too high for the baseline case. This is demonstrated by the simulation under predicting the penetration at 1,480 m/s. The simulations using the TR1a model with parameters fit to the JHB set B boron carbide model demonstrate that reducing the strength of the damaged material increases the penetration and causes an over prediction of the penetration depth. Additionally, simulations using the TR1a model with the JHB set B boron carbide model fit did not predict any dwell at the lower 1,427-m/s impact velocity where it was experimentally observed. For both the TR1 and TR1a simulations of geometry 1 at 1,427 m/s, the majority of the ceramic was damaged

and eligible for granular flow. The difference between the 2 results is due to the difference in the strength of the fragmented material. This demonstrates that the TR1 parameters produce a ceramic that has too little resistance to damage but too much resistance to deformation once it has fragmented. Independent experiments are needed to calibrate both the intact material strength and the damaged material strength. Work is underway to develop a new set of boron carbide material parameters that better fit the response of the Pressure Assisted Densification boron carbide selected as the baseline material for the Materials in Extreme Dynamic Environments Cooperative Research Agreement. It may be possible to calibrate material parameters based on the dwell to penetration transition, as was done for the JHB model,²³ but such an approach undermines the usefulness of the confined ceramic impact experiment as a validation experiment. One should not use the same experimental series for both calibration and validation.

The Eulerian simulations demonstrate that the TR1a and TR2 models can be used in an Eulerian calculation. The TR2 model is faster and more robust but may not be suitable for large elastic deformations. Ceramics are generally not subject to large elastic deformations, and without experimental data to base a model on, there is little reason to retain the added computational expense of the finite elastic deformation model used in TR1 and TR1a for the elastic response of the ceramic. The Eulerian simulations showed better agreement with the experimentally measured penetration depth and the shape of the penetration channel was captured better by the Eulerian simulations. In general, one expects a Lagrangian calculation to do a better job of capturing material interface effects and damage propagation. However, the conversion to SPH particles could be eliminating the strength of the material resulting in a wide-shallow penetration instead of the deep-narrow channel observed in the experiments.

7. Conclusion

This report has presented representative ALE3D simulations using the new Tonge-Ramesh material model.¹ The model performs reasonably well under impact loading conditions up to 4,500 m/s. The model can be significantly accelerated by making some simplifying assumptions about the material behavior and then optimizing the material model to take advantage of these assumptions. The updated (TR2) model is suitable for both Lagrangian and Eulerian simulations and seems to be efficient enough for large simulation problems.

Since the predictions of a simulation are only as good as the material parameters used in the simulation, a new set of boron carbide material parameters should be developed to provide the best fit to existing experimental data. The baseline parameters provide an intact material that is too weak (damage grows too easily) and a failed material that is too strong.

8. References

1. Tonge AL, Ramesh K. Multi-scale defect interactions in high-rate brittle material failure. part I: model formulation and application to ALON. *Journal of the Mechanics and Physics of Solids*. 2016;86:117–149.
2. Tonge AL, Ramesh K. Multi-scale defect interactions in high-rate failure of brittle materials, part II: application to design of protection materials. *Journal of the Mechanics and Physics of Solids*. 2016;86:237–258.
3. Grechka V, Kachanov M. Effective elasticity of rocks with closely spaced and intersecting cracks. *Geophysics*. 2006;71(3):D85–D91.
4. Holmquist TJ, Gerlach CA, Johnson GR. Incorporating the Tonge-Ramesh (TR) ceramic model into the EPIC code. Minneapolis (MN): Southwest Research Institute; 2015 Oct. Technical Report No.: 18.17637.03.
5. Holmquist T, Johnson G. Characterization and evaluation of boron carbide for plate-impact conditions. *Journal of Applied Physics*. 2006;100(9).
6. Fossum AF, Brannon R. On a viscoplastic model for rocks with mechanism-dependent characteristic times. *Acta Geotechnica*. 2006;1(2):89–106.
7. Brannon RM, Leelavanichkul S. A multi-stage return algorithm for solving the classical damage component of constitutive models for rocks, ceramics, and other rock-like media. *International Journal of Fracture*. 2010;163(1):133–149.
8. Brannon RM. Shockwave science and technology reference library. Horie Y, editor. Berlin (Germany): Springer Berlin Heidelberg; 2007. (ShockWave Science and Technology Reference Library).
9. Brannon R, Wells J, Strack O. Validating theories for brittle damage. *Metallurgical and Materials Transactions A: Physical Metallurgy and Materials Science*. 2007;38 A(12):2861–2868.
10. Johnson G, Holmquist T, Beissel S. Response of aluminum nitride (including a phase change) to large strains, high strain rates, and high pressures. *Journal of Applied Physics*. 2003;94(3):1639–1646.

11. Tonge A. Documentation of the Tonge-Ramesh material model for release 2015-06-05-152756. Aberdeen Proving Ground (MD): Army Research Laboratory (US); 2015 Oct. Special Report No.: ARL-SR-0344.
12. Alefeld GE, Potra FA, Shi Y. Algorithm 748: enclosing zeros of continuous functions. *ACM Trans. Math. Softw.* 1995;21(3):327–344.
13. Homel MA, Brannon RM. Relaxing the multi-stage nested return algorithm for curved yield surfaces and nonlinear hardening laws. *International Journal of Fracture.* 2015;194(1):51–57.
14. Coombs WM, Crouch RS, Augarde CE. Reuleaux plasticity: analytical backward Euler stress integration and consistent tangent. *Computer Methods in Applied Mechanics and Engineering.* 2010;199(25–28):1733–1743.
15. Deshpande VS, Gamble EAN, Compton BG, McMeeking RM, Evans AG, Zok FW. A constitutive description of the inelastic response of ceramics. *Journal of the American Ceramic Society.* 2011;94(S1):S204–S214.
16. Bagnold RA. Experiments on a gravity-free dispersion of large solid spheres in a Newtonian fluid under shear. *Proceedings of the Royal Society of London A: Mathematical, Physical and Engineering Sciences.* 1954;225(1160):49–63.
17. Brannon RM. Exact solution for eigenvalues and eigenvectors/projectors of a real 3x3 symmetric matrix. University of Utah, Computational Solid Mechanics Group; 2011 Aug [accessed 2016 Jul 19]. <https://csmbrannon.net/2011/08/29/exact-solution-for-eigenvalues-and-eigenvectorsprojectors-of-a-real-3x3-symmetric-matrix/>.
18. Homel MA, Guilkey JE, Brannon RM. Numerical solution for plasticity models using consistency bisection and a transformed-space closest-point return: a nongradient solution method. *Computational Mechanics.* 2015;56(4):565–584.
19. Brent RP. Algorithms for minimization without derivatives. Mineola (NY): Dover Publications; 2013.
20. Simo JC, Hughes T. Computational inelasticity. 2nd ed. New York (NY): Springer; 2000. (Interdisciplinary Applied Mathematics; vol. 7).

21. Orphal D, Franzen R, Charters A, Menna T, Piekutowski A. Penetration of confined boron carbide targets by tungsten long rods at impact velocities from 1.5 to 5.0 km/s. *International Journal of Impact Engineering*. 1997;19(1):15–29.
22. Westerling L, Lundberg P, Lundberg B. Tungsten long-rod penetration into confined cylinders of boron carbide at and above ordnance velocities. *International Journal of Impact Engineering*. 2001;25(7):703–714.
23. Holmquist T, Johnson G. Response of boron carbide subjected to high-velocity impact. *International Journal of Impact Engineering*. 2008;35(8):742–752.
24. Johnson GR, Holmquist TJ. Test data and computational strength and fracture constants for 23 materials subjected to large strains, high strain rates, and high temperatures. Los Alamos (NM): Los Alamos National Laboratory (US); 1989. Technical Report No.: LA-11466-MS.

INTENTIONALLY LEFT BLANK.

1 (PDF)	DEFENSE TECHNICAL INFORMATION CTR DTIC OCA	44 (PDF)	DIR USARL RDRL WM B FORCH J MCCAULEY S SCHOENFELD RDRL WML H B SCHUSTER B AYDELOTTE RDRL WMM J BEATTY RDRL WMM A E WETZEL RDRL WMM B G GAZONAS D HOPKINS B LOVE B POWERS T BOGETTI RDRL WMM E J SWAB L VARGAS-GONZALEZ J LASALVIA RDRL WMM F T SANO M TSCHOPP RDRL WMM G J ANDZELM RDRL WMP A S BILYK J CAZAMIAS RDRL WMP B C HOPPEL S SATAPATHY M SCHEIDLER A SOKOLOW T WEERASOORIYA J MCDONALD RDRL WMP C R BECKER T BJERKE D CASEM J CLAYTON M GREENFIELD R LEAVY J LLOYD S SEGLETES A TONGE C WILLIAMS RDRL WMP D R DONEY C RANDOW RDRL WMP E S BARTUS
2 (PDF)	DIRECTOR US ARMY RESEARCH LAB RDRL CIO L IMAL HRA MAIL & RECORDS MGMT		
1 (PDF)	GOVT PRINTG OFC A MALHOTRA		
3 (PDF)	JOHNS HOPKINS UNIVERSITY N DAPHALAPURKAR K RAMESH L GRAHAM-BRADY		
1 (PDF)	RUTGERS R HABER		
1 (PDF)	UNIV CALIFORNIA SANTA BARBARA R McMEEKING		
2 (PDF)	LAWRENCE LIVERMORE NATIONAL LABORATORY M HOMEL E HERBOLD		
4 (PDF)	SOUTHWEST RESEARCH INSTITUTE T HOLMQUIST G JOHNSON C GERLACH S BEISSEL		
	<u>ABERDEEN PROVING GROUND</u>		

M BURKINS
P SWOBOWDA
M LOVE
RDRL WMP G
R EHLERS
RDRL VTM
M HAILE